

Full length article

Strengthening and strain hardening mechanisms in a precipitation-hardened high-Mn lightweight steel



M.J. Yao^a, E. Welsch^a, D. Ponge^{a,*}, S.M.H. Haghighat^a, S. Sandlöbes^{a,b}, P. Choi^c,
M. Herbig^a, I. Bleskov^a, T. Hickel^a, M. Lipinska-Chwalek^{d,e}, P. Shanthraj^a, C. Scheu^a,
S. Zaefferer^a, B. Gault^a, D. Raabe^a

^a Max-Planck-Institut für Eisenforschung GmbH, Max-Planck-Str. 1, 40237 Düsseldorf, Germany

^b Institute of Physical Metallurgy and Metal Physics, RWTH Aachen University, 52056 Aachen, Germany

^c Korea Advanced Institute of Science and Technology (KAIST), 291 Daehak-ro, Yuseong-gu, Daejeon, 305-338, Republic of Korea

^d Ernst Ruska-Centre for Microscopy and Spectroscopy with Electrons, Forschungszentrum Jülich GmbH, 52425 Jülich, Germany

^e Central Facility for Electron Microscopy (GFE), RWTH Aachen University, 52074, Aachen, Germany

ARTICLE INFO

Article history:

Received 5 May 2017

Received in revised form

28 July 2017

Accepted 23 August 2017

Keywords:

Lightweight

Precipitation

Strengthening

Strain hardening

Antiphase boundary

ABSTRACT

We report on the strengthening and strain hardening mechanisms in an aged high-Mn lightweight steel (Fe-30.4Mn-8Al-1.2C, wt.%) studied by electron channeling contrast imaging (ECCI), transmission electron microscopy (TEM), atom probe tomography (APT) and correlative TEM/APT. Upon isothermal annealing at 600 °C, nano-sized κ -carbides form, as characterized by TEM and APT. The resultant alloy exhibits high strength and excellent ductility accompanied by a high constant strain hardening rate.

In comparison to the as-quenched κ -free state, the precipitation of κ -carbides leads to a significant increase in yield strength (~480 MPa) without sacrificing much tensile elongation. To study the strengthening and strain hardening behavior of the precipitation-hardened material, deformation microstructures were analyzed at different strain levels. TEM and correlative TEM/APT results show that the κ -carbides are primarily sheared by lattice dislocations, gliding on the typical face-centered-cubic (fcc) slip system $\{111\}\langle 110 \rangle$, leading to particle dissolution and solute segregation. Ordering strengthening is the predominant strengthening mechanism. As the deformation substructure is characterized by planar slip bands, we quantitatively studied the evolution of the slip band spacing during straining to understand the strain hardening behavior. A good agreement between the calculated flow stresses and the experimental data suggests that dynamic slip band refinement is the main strain hardening mechanism. The influence of κ -carbides on mechanical properties is discussed by comparing the results with that of the same alloy in the as-quenched, κ -free state.

© 2017 Acta Materialia Inc. Published by Elsevier Ltd. All rights reserved.

1. Introduction

Al-containing, high-Mn steels exhibit an outstanding combination of strength and ductility enabled by their high strain hardening capacity [1–7]. The addition of aluminum reduces the specific weight of the alloy, hence supporting the notion of lightweight high-Mn steels. Increasing the aluminum content by 1 wt.% yields a reduction in specific weight by about 1.5% [1]. High-Mn lightweight steels usually contain a high content of manganese (18–30 wt.%), aluminum (<12 wt.%) and silicon (<3 wt.%) along with additions of

carbon (0.6–1.8 wt.%) [1–13]. The precipitation characteristics in the Fe-Mn-Al-C system have been investigated in detail in the last decades [10–13]. Due to the strong increase in yield strength in conjunction with a well-maintained tensile ductility upon annealing, the alloy system is a promising lightweight steel candidate for the manufacturing of high performance components.

For alloys containing 5–10 wt.% aluminum, isothermal holding at temperatures between 500 °C and 650 °C for several hours promotes the growth of ordered nano-sized κ -carbides [5,6,12–14]. When the aluminum content exceeds 10 wt.%, κ -carbides already form during quenching from the solution heat treatment temperature [1,15–17]. The κ -carbides cause a significant strengthening, while the good ductility is preserved [4,6,10,14,18]. The κ -carbides are usually finely distributed precipitates of ideally $L/1_2$ -order with

* Corresponding author.

E-mail address: d.ponge@mpie.de (D. Ponge).

an (Fe,Mn)₃AlC stoichiometric composition. However, the chemical composition observed in real alloys usually deviates from this stoichiometry [19,20]. Typically, κ -carbides are coherent or semi-coherent with the disordered austenite matrix with a cube on cube orientation relationship and a lattice misfit of below 2% [21,22]. The precipitation has been proposed to be governed by spinodal decomposition [10,13,23].

Due to the lack of detailed corresponding investigations, the underlying deformation mechanisms causing the extraordinary mechanical properties are thus still unclear. The strain hardening of the as-quenched (AQ) carbide-free state was shown to be caused by the formation of thin slip bands and their gradual, dynamical refinement during straining [24]. The plastic deformation of precipitation-hardened (PH) high-Mn steel is controversially discussed in the literature. While some authors claimed the κ -carbides are sheared by gliding dislocations [6,25], others stated that the κ -carbides are mainly by-passed by the Orowan mechanism [26].

The present investigation aims to clarify the precipitation hardening and the strain hardening mechanisms of these high-Mn lightweight steels by means of electron channeling contrast imaging (ECCI), transmission electron microscopy (TEM), scanning transmission electron microscopy (STEM), atom probe tomography (APT), correlative TEM/APT, and ab initio calculations. The morphology and arrangement of κ -carbide precipitates were analyzed by TEM and APT. While TEM, STEM and correlative TEM/APT were employed to investigate the details of the dislocation/precipitate interaction mechanisms at high resolution, the larger field of view provided by the ECCI technique enabled a quantitative investigation of the strain hardening mechanisms [27,28]. The results of this investigation will be compared to those obtained in a preceding study on the same alloy in the AQ carbide-free state [24] in order to reveal similarities and differences of the associated mechanical properties and deformation mechanisms.

2. Experimental

The chemical composition of the investigated material was Fe-30.4Mn-8Al-1.2C (wt.%). The alloy was melted in an induction furnace and cast in a 12 kg ingot with a thickness of 40 mm under Ar atmosphere. The ingot was reheated to 1200 °C for 30 min and subsequently hot rolled to an engineering thickness reduction of 75% at 1100 °C and then water quenched. From the hot-rolled ingot, bar-shaped samples (11 × 11 × 60 mm³) were cut and solution treated at 1100 °C for 2 h in Ar atmosphere and subsequently quenched in oil. After this solution treatment, cylindrical tensile samples were cut from the bars with gage dimensions of 6 mm in diameter and 40 mm in length. These tensile test samples were then heat treated at 600 °C for 24 h under Ar atmosphere to promote the precipitation of κ -carbides.

The precipitate state after isothermal ageing was characterized by TEM and APT [29]. Discs with a diameter of 3 mm were cut and subsequently grinded to a thickness of ~100 μ m. These discs were then electro-polished by a Struers Tenupol twin-jet device at -30 °C and 10 V using a solution of 30% nitric acid in methanol. Dark-field TEM (DF-TEM) using the (010) superlattice reflection was conducted in a Philips CM20 TEM to observe the κ -carbides. Needle-shaped APT specimens were prepared by focused ion beam (FIB) using a FIB/scanning electron microscopy (SEM) dual beam device FEI Helios Nano-Lab 600i. The usual lift-out procedure [30] was employed. To minimize the Ga implantation into the specimens, the ion beam energy was reduced from 30 kV/~0.26 nA to 16 kV/~0.14 nA after the 1st annular ion milling step and voltage – current values of 2 kV/~24 pA were adopted for final cleaning. Two CAMECA instruments local electrode atom probe (LEAP) devices were used in this work for APT measurements, i.e. the LEAP 3000X-

HR and LEAP 5000X-S [31]. Needle-shaped specimens were analyzed in voltage-pulsing mode at ~70 K at a pulse repetition of 200 kHz, a pulse fraction of 15% and a target evaporation rate of 5 ions per 1000 pulses. The collected APT data were reconstructed and analyzed using the IVAS software (version 3.6.6–3.6.14) by CAMECA instruments.

Tensile tests at room temperature were performed in a Zwick Z100 tensile machine with an initial strain rate of $5 \times 10^{-4} \text{ s}^{-1}$. Besides the tensile tests up to fracture, interrupted tests were also conducted to true strains of $\epsilon = 0.02, 0.05, 0.14$ and 0.27 (equivalent to engineering strains of 2, 5, 15 and 30%, respectively) for studying the microstructure evolution during straining.

The deformation microstructures were characterized using ECCI, TEM, STEM and correlative TEM/APT [32–34]. Cylindrical bulk or thin disc samples at different strain levels were cut from interrupted tensile test samples with the surface perpendicular to the tensile axis, i.e. the observation direction was always along the tensile axis. ECCI was performed using a Zeiss Crossbeam instrument (XB 1540) with a solid-state four-quadrant back-scattered electron (BSE) detector [35]. The working distance was about 6 mm and the acceleration voltage was 30 kV. The orientation of the investigated grains was obtained by electron back-scatter diffraction (EBSD) using an EDAX EBSD system at a working distance of 15 mm and an acceleration voltage of 15 kV. Disc TEM samples were prepared by twin-jet electro-polishing as described above. For imaging dislocations weak-beam dark-field (WB-DF) with the [020] spot was conducted in a Philips CM20 TEM. High resolution imaging was conducted by STEM using a FEI Titan G2 80–200 Cs probe-corrected STEM operated at 200 kV [36]. For the correlative TEM/APT study, electro-polished Mo-grids were used as posts for needle-shaped APT specimens, which could be easily transferred between the FIB, TEM and APT instruments using a grid holder [37,38]. To simplify the TEM measurements and minimize the electron beam damage to APT specimens, needle-shaped specimens are preferred to be orientation-specific. Due to the {001} cube on cube κ/γ orientation relationship, the optimal direction for κ -carbide observation is $\langle 001 \rangle$ while $\langle 011 \rangle$ is the ideal direction to observe particle shearing along the typical fcc-{111} slip planes if it indeed occurs. Therefore, two types of specimens were prepared. With the assistance of preceding EBSD and ECCI observations, orientation-specific specimens were lifted-out from corresponding grains aligned along the corresponding slip line directions, so that the resultant main axis of the needle-shaped specimens directly aligns with the $\langle 001 \rangle$ or $\langle 011 \rangle$ TEM zone axis [39]. In order to minimize beam contamination and surface oxidation, all specimens were freshly prepared just before loading them into TEM double-tilting holders. After the TEM work in the Phillips CM20, the specimens were directly transferred into the FIB for re-sharpening when necessary and a re-cleaning at 2 kV for a few seconds to remove the contamination and oxidized layer. APT measurements were then performed on the fresh specimens with the above-mentioned parameters.

3. Results

3.1. Precipitation state after isothermal annealing

Fig. 1 shows a DF-TEM image of the microstructure after isothermal annealing at 600 °C for 24 h. Well-organized precipitates are observed using the (010) superlattice reflection. This is due to the fact that the $L'_{1/2}$ atomic order of the κ -carbides causes (010) and (110) superlattice spots along the [001] zone axis (see circles in the inset of Fig. 1) [8,12,13,23,40,41].

The dense arrangement of κ -carbides with an average size of

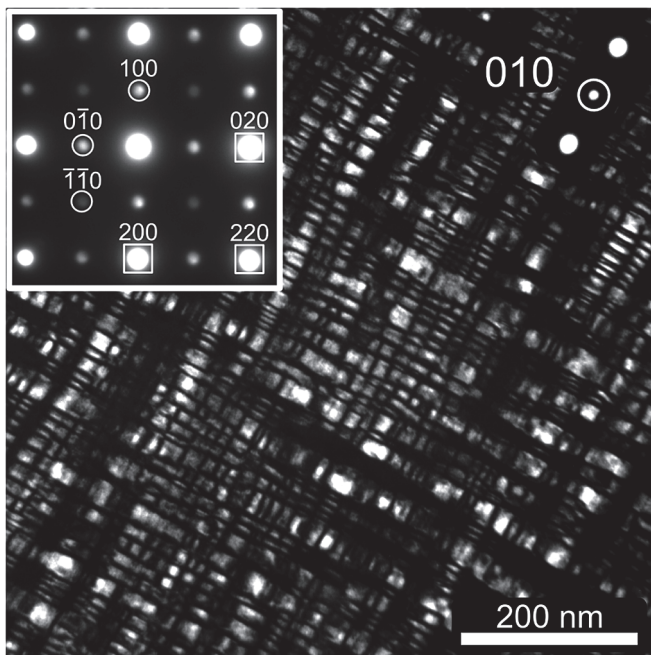


Fig. 1. DF-TEM image of the precipitates using the (010) superlattice spot (highlighted by circle). After isothermal annealing at 600 °C for 24 h well organized nano-sized κ -carbides are observed in the undeformed material. Inset: diffraction pattern along the [001] zone axis. Besides the fundamental fcc spots (marked by squares), additional superlattice reflections (highlighted by circles) indicate the presence of chemically ordered κ -carbides.

about 20 nm is characterized by closely packed cuboids or plates that align preferentially along the elastically soft $\langle 001 \rangle$ directions [20]. Such orientation-specific arrangement of precipitates is frequently observed in the Fe-Mn-Al-C alloy system [11,23,42,43], as well as in Ni-based alloys [44,45] and Co-based alloys [46–48]. With TEM providing a 2D projected image of the microstructure, it is ambiguous to interpret the particle size, shape and inter-spacing from a TEM micrograph alone. To achieve a better topological characterization of the precipitate morphology and arrangement, an additional APT analysis was performed.

Fig. 2(a) shows a representative κ/γ microstructure observed in the reconstructed 3D atom maps by APT, where the κ -carbides are visualized by iso-concentration surfaces encompassing regions where the C composition is above 9 at.%. It is found that in three dimensions, the cuboidal and plate-like κ -carbide precipitates are aligned into particle stacks along the three orthogonal $\langle 001 \rangle$ directions, in agreement with the TEM observations. The cuboidal particles have a size of 15–20 nm. The largest cross-sections of plate-like particles, perpendicular to the particle stack directions, are often square-shaped with an edge length of 15–20 nm, while the thickness of the plates is on the order of 5–10 nm. The particle inter-spacing is small (2–5 nm) between particles within the same stack while the spacing between two parallel stacks is often much larger (10–40 nm). To distinguish these two types of channels, the γ -regions between particles within a stack and between two parallel stacks are correspondingly referred to as narrow and broad γ -channels, respectively. Fig. 2(b) shows a 3D schematic sketch of the κ -carbide precipitates' morphology and arrangement based upon the APT observations. Two possible corresponding 2D intersect-projections along $\langle 001 \rangle$ zone axes, which are often employed for imaging κ -carbides by TEM, are shown in Fig. 2(c). Particles that might be assumed to have a cuboidal morphology based on their square-like appearance in the DF-TEM images have very often a

much smaller size in the third dimension according to APT. Thus, they show plate-like morphology (see the particles outlined in red). At the intersection between two stacks of precipitates a preference for cuboidal morphology is often observed, e.g. the particles outlined in green. Long rectangular particles observed in TEM micrographs (particles outlined in yellow) are found to be rectangular parallelepipeds. The volume fraction of the κ -carbide precipitates in such an alloy was determined approx. 20% [21].

3.2. Plastic yielding and strain hardening performance

Fig. 3 shows the true stress-strain curves at room temperature of the annealed alloy in the PH state. For comparison, the true stress-strain curve of the AQ κ -free state before isothermal annealing is also plotted, which has been studied and described in detail in Ref. [24]. Almost linear flow curves are observed for both cases. The dashed lines show the corresponding strain hardening rates. After isothermal annealing the yield stress is increased by about 480 MPa from the AQ to the PH state while the uniform true strain drops from $\varepsilon = 0.46$ in the AQ state to $\varepsilon = 0.30$ in the PH state. Interestingly, despite the strong increase in yield stress, both high ductility and high strain hardening rate are maintained in the PH state.

At low strains the strain hardening rate for the PH alloy is considerably lower than that in the AQ state, which, however, increases with increasing strain. At a true strain of about $\varepsilon = 0.15$ the strain hardening rates for the two cases are comparable (PH state: $\Theta_{0.15} = 1700$ MPa; AQ state: $\Theta_{0.15} = 1900$ MPa). Hence, after isothermal annealing, not only the yield stress but also the flow stress of the alloy are shifted to higher stresses by about 480 MPa by κ -carbide precipitation.

Similar to the AQ state, the PH alloy shows a non-monotonic course of the strain hardening rate, suggesting the onset of secondary hardening mechanisms at higher loads. The Considère-criterion indicates ductile failure as fracture occurs after necking.

In the PH alloy the strain hardening rate Θ is reduced compared to that in the AQ state, which will be discussed in Section 4.2. The influence of the κ -carbide precipitates on Θ is, however, relatively weaker compared to the strong increase of the flow stress. As a result, the main change in the course of the true stress-strain curve caused by κ -carbide precipitation is the strong increase in flow stress while a good ductility and strong strain hardening capacity are maintained.

3.3. Dislocation/precipitate interactions during deformation

As outlined above in Section 3.2, the κ -carbide precipitates observed in Section 3.1 have a strong influence on the mechanical properties, i.e. they remarkably affect the motion of dislocations. Generally, precipitates affect the deformation substructure compared to the precipitate-free state by Orowan looping or particle cutting [49]. In the current alloy, however, surprisingly very fine and homogeneously distributed slip bands appear as sharp planar crystallographic zones of high dislocation densities that form during straining (highlighted by arrows in Fig. 4(a)). Similar bands were previously reported for the same alloy in the AQ state [24] and also in Refs. [2,17,25,26]. The magnified view in Fig. 4(b) confirms the presence of a high dislocation density within the slip bands. Dislocations in the PH state are strongly curved, which is different from those in the AQ state, where dislocations assembled in slip bands are typically only slightly curved. It should be noted though that the formation of finely dispersed slip bands is observed for both cases.

The pronounced planar slip character in κ -carbide containing high-Mn steels has earlier been discussed on the one hand in terms

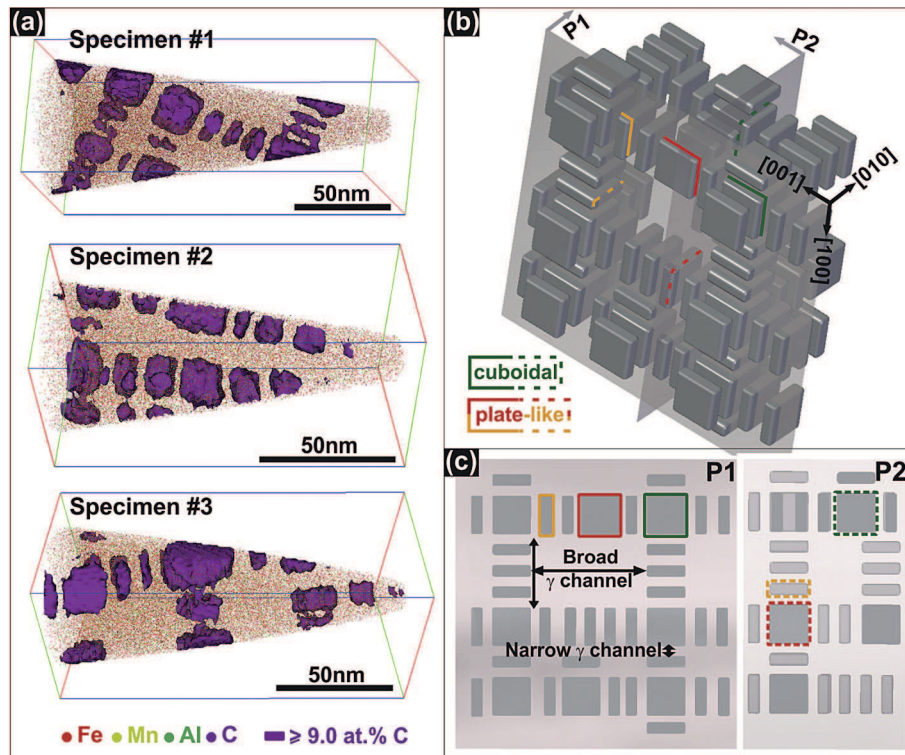


Fig. 2. Morphology and arrangement of κ -carbide precipitates by APT (3D) and 2D sketches: (a) three representative reconstructed 3D APT maps of Fe (red), Mn (yellow), Al (green) and C (purple) atoms. The κ -carbide precipitates are visualized with 9 at.% C iso-concentration surfaces. (b) Schematic illustration of the 3D morphology and arrangement of κ -carbide precipitates based on APT observations. (c) 2D projections of the κ/γ microstructure along $\langle 001 \rangle$ directions highlighted in (b), reflecting the TEM observations. (For interpretation of the references to colour in this figure legend, the reader is referred to the web version of this article.)

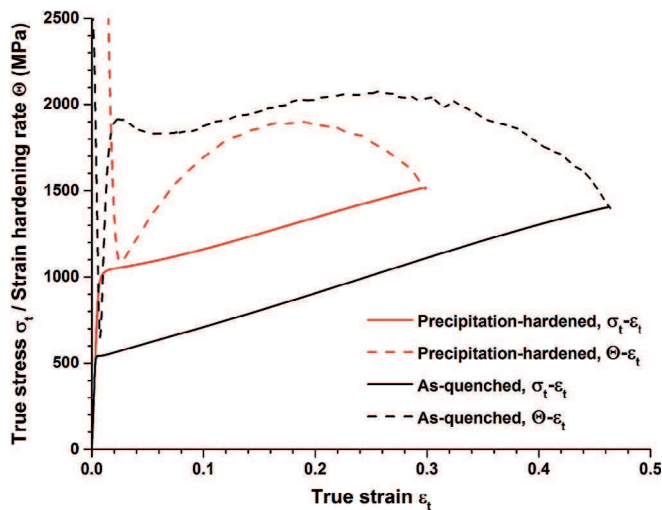


Fig. 3. True stress-strain curve of the alloy in precipitation-hardened state (red solid line) in comparison to that of the alloy in the as-quenched state (black solid line). The strain hardening curves Θ of both states are shown as dashed lines. (For interpretation of the references to colour in this figure legend, the reader is referred to the web version of this article.)

of “glide plane softening” caused by shearing of the precipitates [6,25], while on the other hand it was ascribed to the presence of the varying spacing between precipitates forming preferential glide concentration pathways [26]. Due to the lack of a detailed investigation, the dislocation/ κ -carbide interaction mechanism is still unclear. Therefore, further TEM and correlative TEM/APT studies were conducted on deformed PH samples under various strain

states.

Fig. 5 shows the DF-TEM micrographs of a sample deformed at a true strain of 0.02 using the (010) superlattice reflection close to the [110] zone axis. The whole precipitation structure is shown to be sheared along a fine line, indicating the shearing of κ -carbide precipitates by dislocations on the same glide plane. Shearing of a similar precipitate morphology has been reported in Ni-base superalloys, where the deformation structure is also characterized by fine planar slip bands [45,50–53]. They attribute the planar slip character to the presence of short-range order and to the shearing process of ordered γ' precipitates [45,50–53].

More highly strained microstructures are shown in Fig. 6 that displays TEM micrographs obtained from needle-shaped APT specimens. At a strain level of 0.05, clear shearing of κ -carbide stacks is also observed along the [011] zone axis as indicated by the arrows in Fig. 6(a). The κ -carbide precipitates have a (001) cube on cube orientation relationship with the γ -matrix. Along the [011] zone axis, i.e. taking a view edge-on the (11 $\bar{1}$) plane, the nanometer-sized κ -carbides with a 2–5 nm inter-spacing in the narrow γ -channels overlap with each other in the 2D TEM projection. Instead of individual precipitates, a line of precipitates is observed. Misalignments of several stacks along a single slip line are captured (Fig. 6(a)), clearly revealing the shearing of κ -carbides by slip. As the true strain increases to 0.15, more slip systems are activated and intense slip bands appear (highlighted by arrows in Fig. 6(b)), which, along the [001] zone axis, are also manifested by the formation of densely arranged precipitate fragments concentrating along specific directions. In comparison to the relatively complete precipitates at the apex of the needle-shaped specimen, the κ -carbide precipitates within these slip bands are fragmented into small debris. At the intersection of slip bands, the superlattice

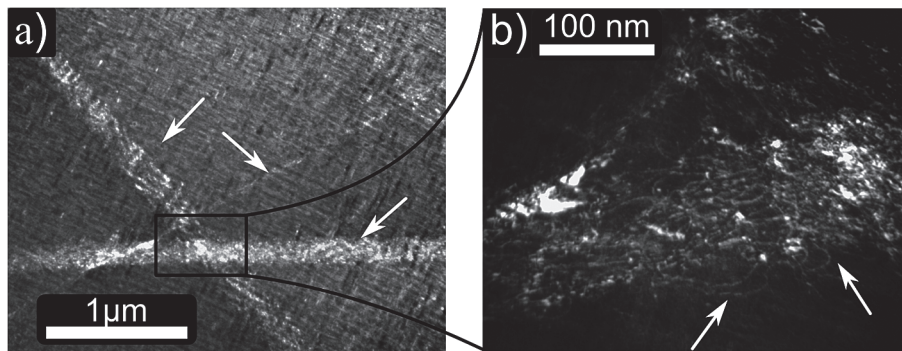


Fig. 4. TEM images revealing slip bands in the $\varepsilon = 0.02$ deformed alloy: (a) an overview of three non-coplanar slip bands (marked by arrows); (b) the slip bands consist of strongly curved dislocations that glide on the same $\{111\}$ glide plane (see plane traces in Fig. 9a). The “width” of the bands in this image is due to projection effect since the slip bands are observed under a certain inclination angle. This inclination determines how thick the slip bands appear in the 2D projected TEM image.

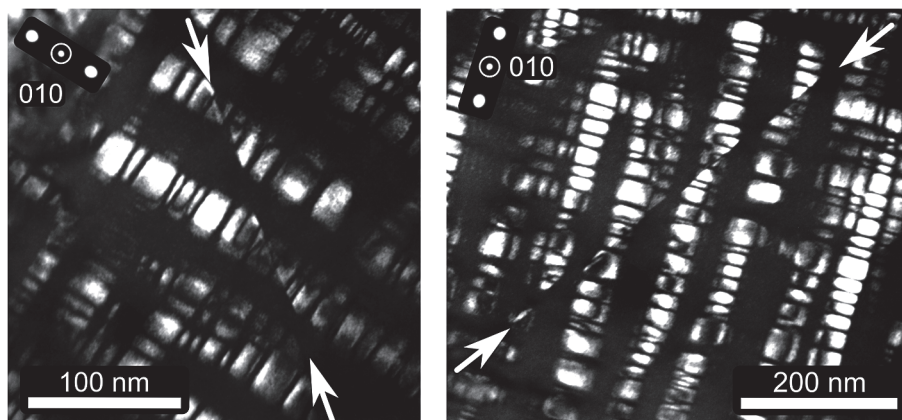


Fig. 5. DF-TEM images showing sheared κ -carbides at a true strain of 0.02 (with $g=(010)$ superlattice reflection used for DF imaging and viewing direction close to the $[110]$ zone axis). The precipitation structure is sheared along a sharp line indicating the passage of many dislocations on the same glide plane.

phase contrast is almost completely lost, indicating either the loss of ordering or even dissolution of precipitates.

Shearing of κ -carbide precipitates by slip bands are observed from low-strain to high-strain states and from different zone axes, not only in the representative examples shown in Figs. 5 and 6, but also in another 10 needle-shaped specimens. Therefore, particle shearing is therefore a general phenomenon observed in the deformed κ/γ microstructure and believed to be the prevalent deformation mechanism in the studied alloy. The previous debates in the literature on the mechanism (shearing or Orowan looping) are probably due to the lack of a clear observation of such deformed microstructures, especially at high strains. The high density of particles and specific crystallographic orientation make the investigation difficult. Here, these difficulties are circumvented by optimized specimen preparation, adopting thin needle-shaped specimens specifically oriented with the help of a prior EBSD measurement.

The mapping of the deformed microstructure along with the 3D atomic-scale chemical mappings, accomplished by correlative TEM/APT on a single specimen at a true strain of 0.15, is presented in Fig. 7. In the TEM micrograph (Fig. 7(a)), two originally cuboidal or plate-like κ -carbide precipitates have been clearly split into two parts - one major part and another smaller one at the corner, as highlighted by blue arrows. The slight mismatch between these two parts, particularly for the right plate-like κ -carbide, indicates that these two precipitates had been sheared by dislocation slip. The slip directions of the two precipitates are parallel to each other. Since the needle-shaped specimen is prepared orthogonally along

the $\langle 001 \rangle$ direction, the slip direction can be characterized as $\sim 45^\circ$ from $[001]$ and $[010]$, i.e. close to $[011]$. Also, as highlighted by yellow arrows, there are some small fragments stemming from the ordered precipitates, which probably have been heavily fragmented by deformation.

The same specimen was subsequently analyzed by APT. Fig. 7(b) shows an overlay of the reconstructed APT analysis volume on top of the DF-TEM micrograph. The latter utilizes the superlattice diffraction contrast to reveal the ordered κ -carbide precipitates whereas the former employs carbon iso-concentration surfaces at a threshold value of 9.0 at.% to show the carbon-enriched κ -carbides. The size, shape and position of κ -carbide precipitates in the reconstructed APT volume fit well with the DF-TEM image. The particle splitting by dislocation slip is not clearly observed by APT, conversely to what was highlighted by blue arrows in the DF-TEM image (Fig. 7(a)). This is probably due to shearing of the precipitate by the glide of only one single dislocation rather than dense slip bands of high dislocation density, as captured in the TEM micrograph (Fig. 6(b)). The signal is likely smoothed out by voxelization and delocalization of APT data. Therefore, instead of two split parts pertaining to one initial precipitate, only one complete κ -carbide is visualized by the carbon iso-concentration surface in the probed APT volume. In addition to the large κ -carbides observed in both, TEM and APT, there are also small, irregularly shaped fragments with no obvious visual match between TEM (Fig. 7(a)) and APT (Fig. 7(c)) measurements: the region of which is marked by a black dash circle in Fig. 7(c). Some fragments observed in the DF-TEM image are not found in APT analysis via 9.0 at.% C iso-

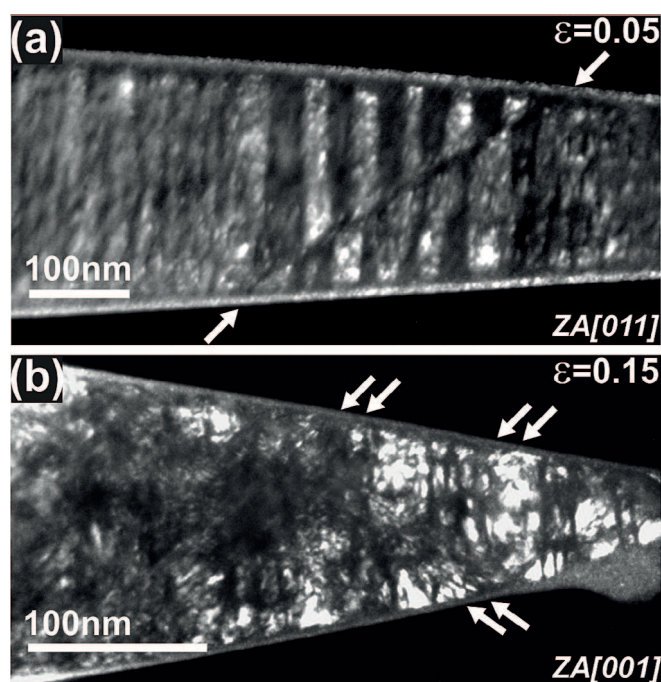


Fig. 6. DF-TEM images of deformed microstructures at different true strains of (a) $\epsilon = 0.05$ and (b) $\epsilon = 0.15$ utilizing the superlattice diffraction spot of κ -carbides. Two different zone axes (ZA) (a) [011] and (b) [001] were employed to show the shearing of κ -carbides and sheared κ -carbides, respectively.

concentration surface, and vice versa. This is probably due to the limited field-of-view of APT so that the outer shell of the specimen observed in TEM are not registered by the APT detector, which can be recognized by the image overlay in Fig. 7(b) and has also been reported in Ref. [37].

To better reveal the 3D solute distribution in the matrix after deformation, further APT elemental maps and iso-concentration surfaces of different elements at varying threshold values were reconstructed from the data (Fig. 7(c–e)). In the region surrounded by the black dashed circle in Fig. 7(c), the elements are not homogeneously distributed. A lower threshold value for the C iso-concentration surface of 7.5 at.% unveils that there are not only small C-enriched fragments but also C segregation along certain directions, as indicated by black arrows in Fig. 7(d). Such a linear solute enrichment is also found for Al at the same positions (Fig. 7(e)), but not for Mn (not shown here). Completely differing from the common particle morphology (Fig. 2(a)), these line features imply that the κ -carbides in this region have been fragmented and dissolved during deformation. The dislocation slip might have destroyed the κ -carbides and dragged solutes along with it [54–56]. Considering the affinity between segregated solutes and crystalline defects [57], it is highly possible that the solute segregation zones are dislocation lines [58,59]. The reason why such an enrichment only takes place for Al and C, and not for Mn, is that the κ -carbides are enriched in Al and C, but not in Mn [19].

Owing to the $\langle 001 \rangle$ -oriented specimen, as well as the (001) cube on cube orientation relationship between κ -carbide precipitates and γ -matrix, the $\langle 001 \rangle$ directions can be easily identified for the reconstructed 3D APT analysis volume (Fig. 8). Therefore, a crystallographic analysis can be performed on the linear solute segregation zones, highlighted by black arrows in Fig. 7(d).

All three linear segregation zones (Fig. 8(a), (b) and (c)) are well associated to {111} planes, which are the slip planes in fcc metals. Along with the aforementioned $\langle 110 \rangle$ slip direction (Fig. 7(a)), the activated slip system can be identified as $\{111\}\langle 110 \rangle$, that is the typical slip system in fcc metals. Among these three linear segregation zones, one line is found to be perpendicular to the $\langle 110 \rangle$ slip direction (Fig. 8(a)) and the other two are inclined relative to this direction (Fig. 8(b), (c)), which implies that the former is probably an edge dislocation while the latter is of mixed dislocation

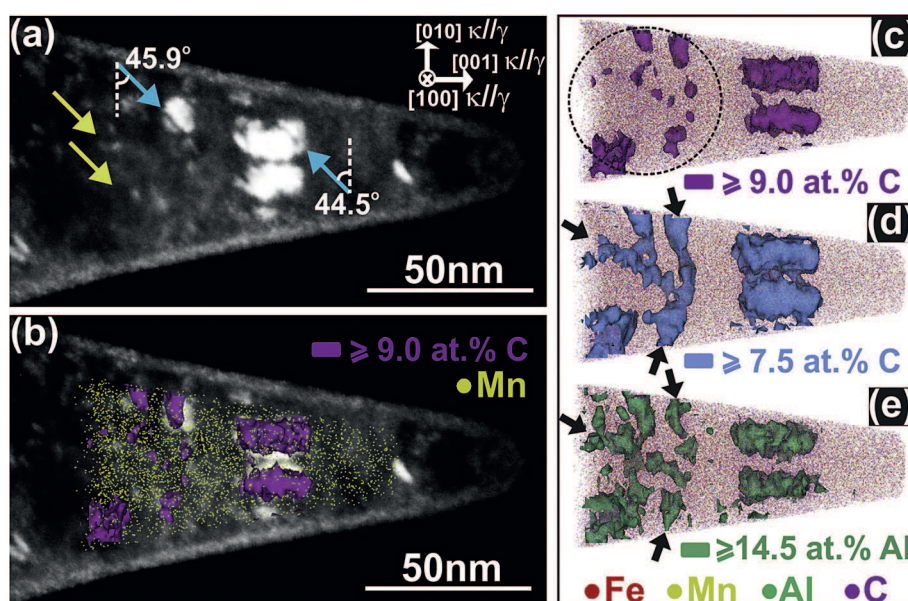


Fig. 7. Correlative TEM/APT analysis of a deformed microstructure at a true strain of $\epsilon = 0.15$: (a) DF-TEM micrograph along [001] zone axis with the blue arrows highlighting the shearing of κ -carbides and yellow ones indicating the fragments of κ -carbides; (b) overlay of the reconstructed APT analysis volume with purple κ -carbides visualized by carbon iso-concentration surfaces at a threshold value of 9.0 at.% on top of the DF-TEM micrograph of the same specimen taken before APT measurement; (c–e) 3D elemental atom maps of the reconstructed APT volume with different elemental iso-concentration surfaces of (c) $C \geq 9.0$ at.%, (d) $C \geq 7.5$ at.% and (e) $Al \geq 14.5$ at.%, showing the deformation-driven dissolution of κ -carbides. The dashed black circle highlights the inhomogeneity of C atoms while the black arrows mark the linear solute segregations. (For interpretation of the references to colour in this figure legend, the reader is referred to the web version of this article.)

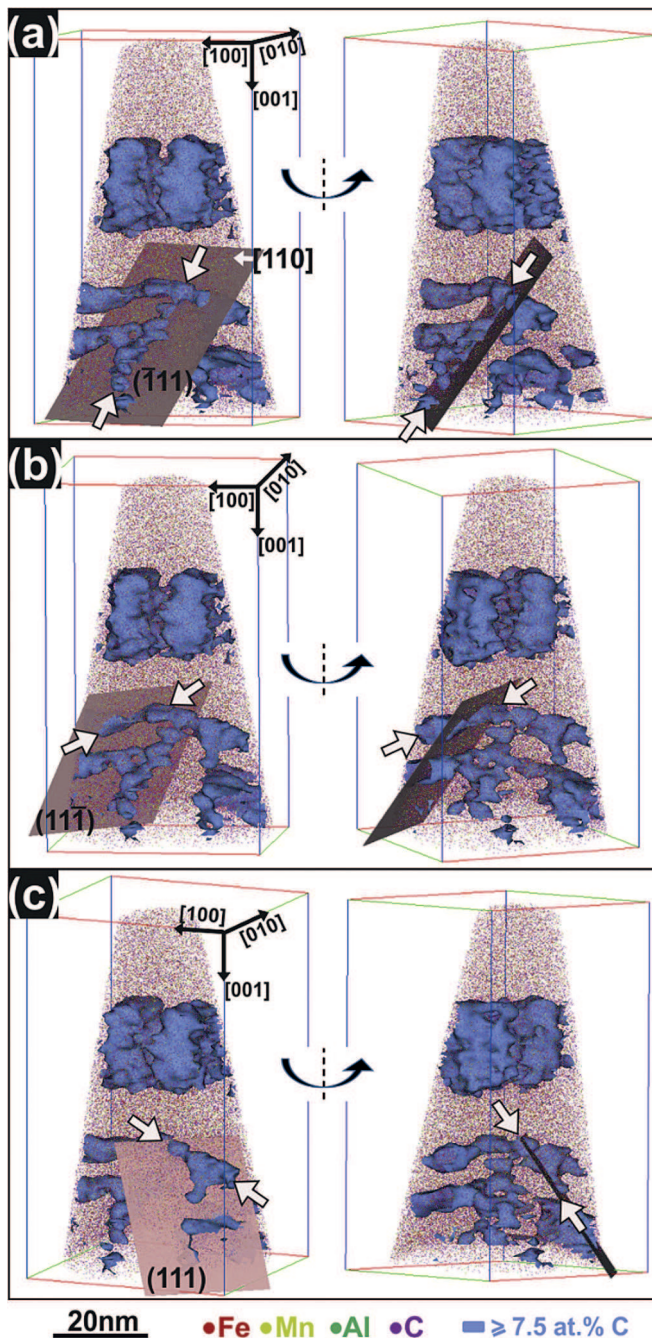


Fig. 8. Crystallographic analysis of three solute-segregated line features in a deformed κ/γ alloy at a true strain of 0.15 as highlighted by black arrows in Fig. 7(d) based on the orientation of the needle-shaped specimen.

character.

3.4. Evolution of the deformation structure

Fig. 9 shows that the evolution of the deformation substructure at various true strains ($\epsilon = 0.02, 0.05, 0.14, 0.27$) is characterized by the formation of slip bands during straining. The tensile axis is perpendicular to the image plane in all ECCI images. At a true strain of $\epsilon = 0.02$ (Fig. 9(a)) the structure is characterized by fine slip bands, as shown in the TEM micrograph in Figs. 4 and 5. Between the slip bands the interface strain between the κ -carbides and the disordered matrix gives rise to modulated contrast (misfit is below

2%). At a true strain of $\epsilon = 0.05$ (Fig. 9(b)) the deformation substructure has not changed qualitatively, however, the spacing between the slip bands has been considerably reduced. The micrographs in Fig. 9(c) and (d) show the deformation structures at $\epsilon = 0.14$ and $\epsilon = 0.27$, respectively. The spacing between the slip bands has been further reduced, while the character of the deformation structure has been maintained. Slip bands generally extend throughout the entire grains, indicating weak obstacle forces acting at intersecting slip bands, as slip bands continue propagating by cutting through intersecting slip bands.

The observed deformation structure shows strong similarities to the structures reported before about the same AQ alloy [24]. The formation of slip bands and the occurrence of dislocations on individual $\{111\}$ planes in the deformation structure of the current age hardened alloy are also attributed to pronounced planar glide (see plane traces in Fig. 9(a)). The role of κ -carbide precipitates on the distribution of slip bands will be discussed in Section 4.2.

In order to quantify the observed slip band refinement shown in Fig. 9, a slip band analysis has been conducted, where the distances among the slip bands has been measured by ECCI in several grains (about 30 measurements per deformation state) at four different true strains ($\epsilon = 0.02, 0.05, 0.14, 0.27$). Details on the slip band analysis are given elsewhere [24]. The error bars indicate the inhomogeneities in the deformation microstructure originating from locally varying stress states within the sample [60–63]. Fig. 10 shows the resultant mean slip band spacing as a function of strain level along with that found for the same material in the AQ state, taken from Ref. [24]. The reduction of the slip band spacing during straining, which we observed qualitatively in Fig. 9, is clearly reflected in the diagram.

4. Discussion

4.1. Strengthening mechanisms

The precipitation of κ -carbides is found to significantly strengthen the alloy (Fig. 3). The deformed microstructure of the PH alloy has been studied by ECCI, TEM and correlative TEM/APT. It is revealed that $\{111\}\langle 110 \rangle$ dislocation slip and shearing of κ -carbide precipitates primarily occurs during plastic deformation.

The ordered κ -carbide with an L'_{12} -type perovskite structure deforms differently from the disordered fcc γ -matrix. For dislocation slip on a crystallographic plane, a shear stress, the so-called Peierls stress, has to be exerted on the slip plane, which depends exponentially on the ratio of lattice spacing d to the Burgers vector b and therefore ought to be smallest for slip along the close-packed direction on the close-packed plane [64]. In disordered fcc γ , this corresponds to the $a/2\langle 1\bar{1}0 \rangle\{111\}$ slip system (a is the lattice parameter). However, in chemically ordered L'_{12} κ -carbides, the preferred slip system could be $a\langle 100 \rangle\{001\}$ or $a\langle 1\bar{1}0 \rangle\{111\}$, since the shortest lattice vectors $a\langle 100 \rangle$ do not lie in the close-packed $\{111\}$ planes. The experimentally observed activated slip system is the latter. Given that the Burgers vector of a perfect dislocation in the γ -matrix ($a/2\langle 1\bar{1}0 \rangle$) is only half of the closing vector to restore the ordered κ -carbide to its perfect lattice, it cannot enter the κ -carbide unless a planar defect is formed [65,66]. The resultant planar fault in-between two super-partials is known as an anti-phase boundary (APB) and the APB energy γ_{APB} represents the associated energy barrier for the occurrence of particle cutting. If the system wants to avoid formation of an APB, a pair of super-partial $a/2\langle 1\bar{1}0 \rangle\{111\}$ dislocations must travel together through the κ -carbides, forming a so-called superdislocation.

The strength of the coupling between a pair of super-partial dislocations, for a given volume fraction, V_f , depends on the mean

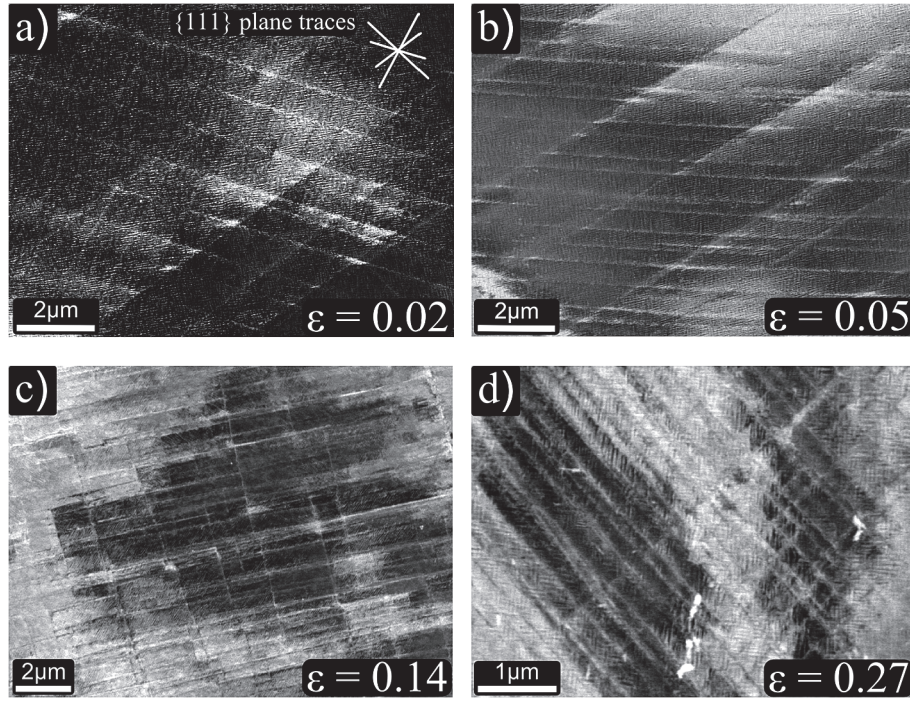


Fig. 9. ECI images of the deformation microstructures at different strain levels, characterized by finely dispersed slip bands. With increasing the true strains, the spacing between the slip bands gradually decreases (see quantification in Fig. 10). No deformation twins are observed even at high strains. All image planes are perpendicular to the tensile axis.

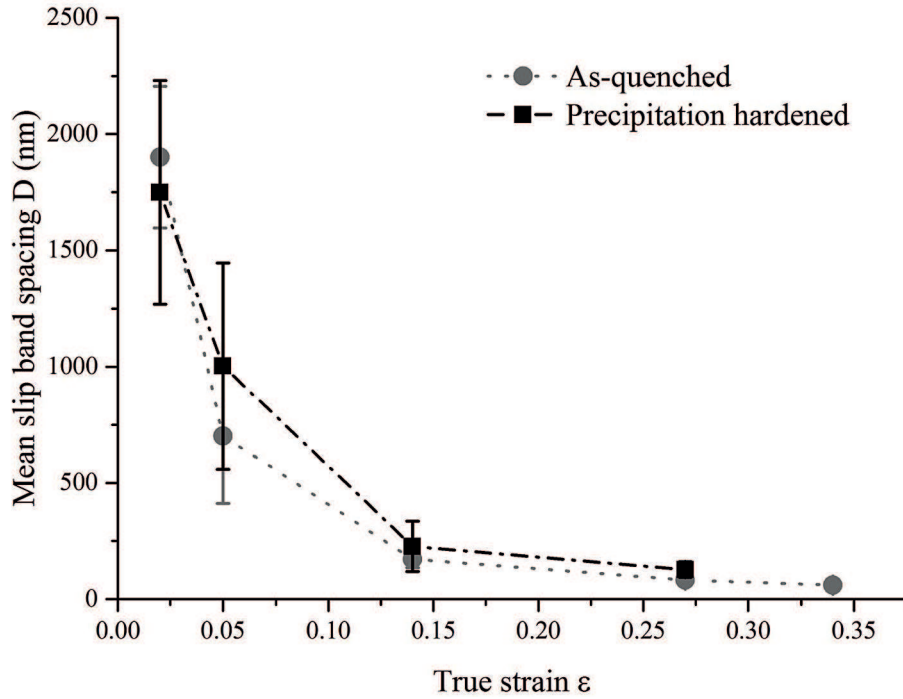


Fig. 10. Evolution of the mean slip band spacing D during straining for the studied precipitation-hardened material together with data obtained for the same alloy in the as-quenched state [24] for comparison. The mean slip band spacing decreases during straining similarly in both cases. The error bars are caused by inhomogeneities in the deformation microstructure.

particle radius, r , and γ_{APB} [66]. For small particle sizes, i.e. $r\gamma_{APB} \ll Gb^2$, the super-partials are weakly coupled, and the stress required for a single weakly coupled super-partial dislocation to shear a κ -carbide particle is given by

$$\Delta\sigma_{prec} = M \frac{\gamma}{2b} \sqrt{V_f} \left[\sqrt{\frac{12\gamma_{APB}r}{\pi Gb^2}} - \sqrt{V_f} \right]. \quad (1)$$

Similarly, for intermediate size particles, i.e. $r\gamma_{APB} \gg Gb^2$, the

super-partials are strongly coupled, and the resulting particle shearing stress is given by

$$\Delta\sigma_{prec} = M\sqrt{\frac{3}{2}}\left(\frac{Gb}{r}\right)\sqrt{V_f}\frac{w}{\sqrt{\pi^3}}\left(\frac{2\pi\gamma_{APB}r}{wGb^2}-1\right)^{\frac{1}{2}}, \quad (2)$$

where M is the Taylor factor of 3.06 to convert the resolved shear strength for dislocation motion into an equivalent uniaxial yield strength of a polycrystal [67], G represents the shear modulus, b denotes the magnitude of the Burgers vector and w is a dimensionless constant of the order of unity. Thus, with increasing particle size, an increased strengthening effect is observed in the weakly coupled regime, i.e. $\Delta\sigma_{prec} \propto \sqrt{r}$, while a decreased strengthening effect is observed in the strongly coupled regime, i.e. $\Delta\sigma_{prec} \propto 1/\sqrt{r}$, with the peak strength of $\Delta\sigma_{prec} \sim M\sqrt{V_f}\gamma/2b$ occurring at the transition radius of $r \sim Gb^2/\gamma_{APB}$. As $r \rightarrow \infty$, the Orowan mechanism,

$$\Delta\sigma_{prec} = M\left(\frac{Gb}{2r}\right)\left(\sqrt{\frac{2\pi}{3V_f}}-2\right)^{-1}, \quad (3)$$

is predominant, resulting in $\Delta\sigma_{prec} \propto 1/r$.

To quantify the strengthening, the APB energy of the $L'1_2$ -type (Fe,Mn)₃AlC κ -carbides has been determined by ab-initio calculations in this work. The VASP code [68] has been used in conjunction with the projector-augmented wave (PAW) method [69] and the generalized gradient approximation [70], a plane wave energy cut-off of 400 eV, and a k -mesh corresponding to 16000 k -points per atom. To avoid probing a large amount of configurations, the ordered ternary Fe₃AlC κ -carbide, rather than partially quaternary (Fe,Mn)₃AlC κ -carbide is used for the calculation of the APB energy. Since the C content of κ -carbide precipitates in high-Mn lightweight steels has been found to be significantly below the stoichiometric value [20], two extreme cases have been studied, namely, a full occupancy of the body-centered interstitial sites by C and a C-free $L'1_2$ Fe₃Al structure. Though substitutional Mn_{Al} anti-site defects have also been reported [19], they are less important here and are hence not taken into account for simplicity. The APB energetic calculations have been performed at the experimental lattice constant (3.68 Å) [19].

Since the APB in a κ -carbide is also an extended planar fault of {111} planes, the concepts of stacking fault energy calculations in steels can be applied [71–76]. Hence, the energetics of an APB can be obtained from a generalized extended energy surface, called γ -surface, which is defined by shearing two parts of the crystal with respect to one another along {111} planes. Similar to [72], the unit cell of the κ -carbide with the $L'1_2$ structure is defined such that the unit vectors **a** and **b** span the {111} planes (Fig. 11(a–c)). This cell contains 9 Fe, 3 Al, and 3 C atoms. A repetition of the cell in the **c** direction yields the supercell (Fig. 11(d)), which is subsequently tilted to accommodate shears of the upper half of the crystal with respect to the lower one (Fig. 11(e), without C). The Gibbs free energy difference between the ideal and the sheared cell, $\gamma = (G^{\text{def}} - G^{\text{ideal}})/A_{\text{int}}$, defines the γ -surface, where A_{int} is the interface area over which the defect extends. An APB structure is obtained for the two shears (I) $1/2\mathbf{a}$ (or equivalently $1/2\mathbf{b}$) and (II) $1/2(\mathbf{a}+\mathbf{b}) = 1/2\mathbf{u}$, yielding local minima on this energy landscape that correspond to γ_{APB} .

The results obtained for the two extreme compositions (with and without C) and for the two types of shearing (I. $1/2\mathbf{a}$ (or $1/2\mathbf{b}$) and II. $1/2\mathbf{u}$), are summarized in Table 1. The calculations have been performed with and without taking the relaxation of atomic positions next to the APB into account. It is found that there is negligible

energetic difference between type I and type II shearing. The APB energies are also not significantly affected by relaxation when there is no C; whereas in the presence of C, the energies are clearly lower in the relaxed case in comparison to those without relaxation. More importantly, however, the C concentration of the κ -carbide is found to have a remarkable influence on the APB energy: the stoichiometric composition, i.e. full occupation of C sites, has an APB energy about 3 times of that of the scenario without C. Instead of a stoichiometric C composition of 20 at.%, the actual C concentration of the κ -carbide is in the order of 13 at.% [20]. Therefore, the γ_{APB} value of the κ -carbide in the current alloy is expected to lie in the range of ~350–700 mJ/m². It is also worth noting that this value is much higher than for γ' precipitates in superalloys (~100 mJ/m²) [66].

Taking $G = 70$ GPa, $b = 0.26$ nm [24], and $\gamma_{APB} \sim 350$ –700 mJ/m², the transition between the weakly and strongly coupled regimes is estimated to occur at particle radii ranging from $r \sim Gb^2/\gamma_{APB} = 6.8 - 13.5$ nm. The measured particle radius of $r = 10$ nm (Section 3.1) indicates that for the given volume fraction, $V_f \sim 0.2$ (Section 3.1), the strengthening is close to the peak value of $\Delta\sigma_{prec} \sim 0.9 - 1.8$ GPa. However, experimentally, the ageing-introduced κ -carbides were found to increase the yield strength of the alloy only by ~500 MPa (Section 3.2).

This discrepancy might be explained by the influence of dislocation pile-up stresses at the κ -carbide interfaces that assist particle shearing. The pile-up of dislocations in the grain interior has been observed in the AQ state with short range ordering [24], which however is difficult to be captured here in the PH state, with its high number density of precipitates by ECCI or TEM. Yet, when considering a pile-up of N dislocations, the forces controlling the onset of particle shearing on the i^{th} dislocation adjacent to the hetero-interface between matrix and precipitate can be expressed as

$$\frac{\Delta\sigma_{prec}}{M}bL + \sum_{j \neq i} R_{ij} = F_i, \quad (4)$$

where, $L = r\sqrt{2\pi/3V_f}$ is the inter-particle spacing, M is again the Taylor factor, $R_{ij} = wGb^2l/2\pi(x_i - x_j)$ are the elastic interaction forces between the i^{th} and j^{th} dislocation with position x_i and x_j , respectively, and $F_i = \gamma_{APB}l$ is the force of the particle for dislocation line length inside the particle, l . At the maximum load configuration of incipient particle shearing by the leading dislocation, $F_i = 0$ for all $i \neq 1$. Since $R_{ij} = -R_{ji}$, summing over all forces in equation (4) yields the identity,

$$N\frac{\Delta\sigma_{prec}}{M}bL = \gamma_{APB}l. \quad (5)$$

Furthermore, due to the high value of γ_{APB} , it is expected that the separation between the leading dislocation pair will be very small compared with the separation to the remaining dislocations in the pile-up, i.e. $|x_1 - x_2| \ll |x_1 - x_j|$ for $2 \leq j \leq N$. Under these conditions, since $R_{1j} \sim R_{2j}$, force equilibrium between the leading dislocation pair yields the second identity,

$$2R_{12} = 2w\frac{Gb^2}{2\pi}\frac{l}{\Delta x} = \gamma_{APB}l. \quad (6)$$

Solving equation (6) for the leading dislocation pair spacing, $\Delta x = x_1 - x_2$, and using the relation for spherical particles, namely, $l = 2\sqrt{2r\Delta x - \Delta x^2}$ in equation (5) results in the following modified form of the strengthening in the presence of a dislocation pile-up of size N

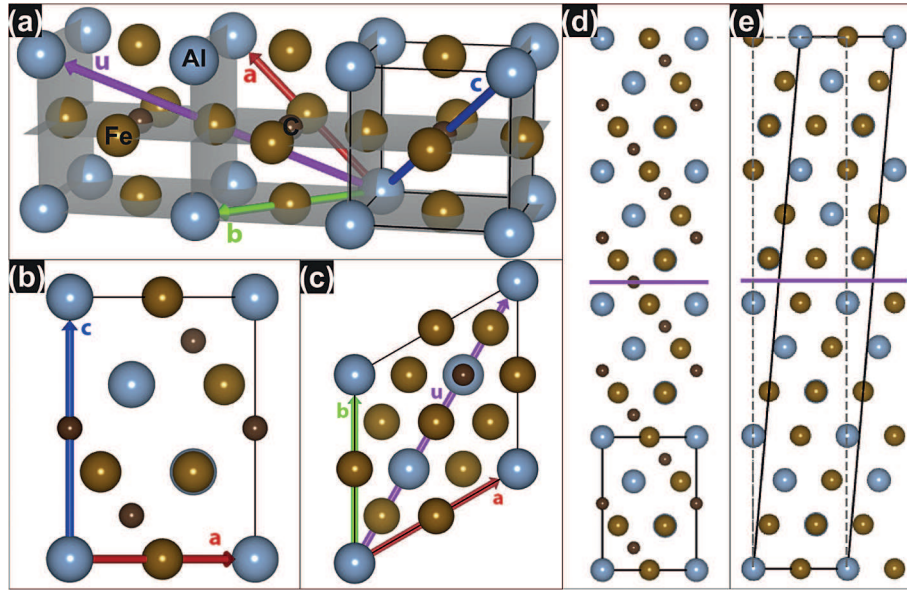


Fig. 11. Schematic illustration of supercells of κ -carbide used for APB energy calculations. (a–c) different perspectives of the applied unit cell of the κ -carbide with unit vectors **a**, **b**, **c**. (d) the supercell containing C that is not sheared; (e) the supercell without C that is sheared by $1/2\mathbf{a}$; the pink lines mark the planes along which the two portions of the crystal are sheared with respect to the another.

Table 1
Ab initio calculated APB energies based on the supercells in Fig. 11.

APB type		APB energies [mJ/m ²]	
composition	APB shift type	unrelaxed	relaxed
without C	II. $1/2\mathbf{u}$	363	344
without C	I. $1/2\mathbf{a}$ (or $1/2\mathbf{b}$)	364	347
with C	II	1029	862
with C	I	1029	826

$$\Delta\sigma_{prec} = \frac{M}{N} \sqrt{\frac{3}{2}} \left(\frac{Gb}{r} \right) \sqrt{V_f} \frac{2w}{\sqrt{\pi^3}} \left(\frac{2\pi \gamma_{APB} r}{w G b^2} - 1 \right)^{\frac{1}{2}}, \quad (7)$$

and a modified peak strength of, $N\Delta\sigma_{prec} \sim M\sqrt{V_f}\gamma/b$. This indicates that a pile-up size of 4–8 dislocations is required to reduce the macroscopic strengthening effect to ~500 MPa, which, based on previous experimental observations [24], is a reasonable assumption.

It is well known that for coherent particles both mechanisms, i.e. particle shearing or Orowan looping, can in principle be activated, depending on particle size, interspacing, interfacial energy, elastic misfit and antiphase boundary energy. Considering the small κ/γ lattice misfit, the interfacial energy is relatively negligible in comparison to the high APB energy. Therefore, in Fig. 12, the normalized strengthening, $N\Delta\sigma_{prec}/\sqrt{V_f}$, is plotted as a function of the mean particle radius for $\gamma_{APB} \sim 350\text{--}700$ mJ/m². In general, as the particle size r increases, the active mechanism changes from weakly coupled particle shearing to strongly coupled particle shearing and in the end to Orowan looping. One should note that an increase of γ_{APB} from 350 mJ/m² to 700 mJ/m² has several effects, namely, (i) increasing the peak stress, (ii) decreasing the radius at which transition from weakly coupled to strongly coupled particle shearing occurs, and (iii) decreasing the critical particle radius at which Orowan looping becomes the prevalent mechanism from 38 nm to 19 nm. Considering the particle size of ~10 nm in the current PH alloy, we conclude that particle shearing is the

predominant mechanism during deformation while depending on the exact γ_{APB} and specific particle size, superdislocation cutting through the particles could be either strongly coupled or weakly coupled.

In Section 3.1 we have shown that although in TEM the κ -carbide precipitates seem to be distributed homogeneously (Fig. 1), 3D topological analysis reveals they are arranged rather inhomogeneously, with clearly discernible broader and narrower γ channels (Fig. 2). Hence, in addition to Fig. 12, where a homogeneous distribution of precipitates has been assumed with a certain volume fraction, we further studied the influence of particle interspacing on the stresses for the different mechanisms. As shown in Fig. 13, the Orowan mechanism is more sensitive to particle interspacing than the shearing mechanisms, in particular at low particle interspacing values. When γ_{APB} has a high value of 700 mJ/m², the Orowan mechanism is preferred if a channel spacing is larger than ~20 nm; while for $\gamma_{APB} = 350$ mJ/m², the critical channel size is about 60 nm. According to the current APT analysis (e.g. Fig. 2), the broader γ channels are found to be in the range of 10–40 nm while the narrower γ channels are of the order of 2–5 nm. When dislocations are squeezed into these narrow channels, bowing out through the channels is unlikely owing to the inverse relation between stress and channel width and thus cutting through the particles by superdislocations is preferred. Since locally the broad channel spacing (10–40 nm) might be larger than the critical channel spacing for the activation of the Orowan mechanism at high γ_{APB} values (~20 nm), we do not completely rule out the occurrence of Orowan looping in some local regions with relatively wide particle interspacing. It could for instance indeed take place in the more broadly spaced channel regions that were observed to occur among aligned groups of particles (i.e. particle stacks), as shown in Fig. 14(a and b). This assumption explains the strongly curved dislocations shown in Fig. 4(b) and in Ref. [26]. However, it is also worth noting that the arrangement of κ -carbides in the form of stacks that are orthogonally aligned along all $\langle 001 \rangle$ directions, which suggests that although there is a broad γ space which might have triggered Orowan looping, about 10–40 nm away there are also κ -carbide stacks with more narrow internal

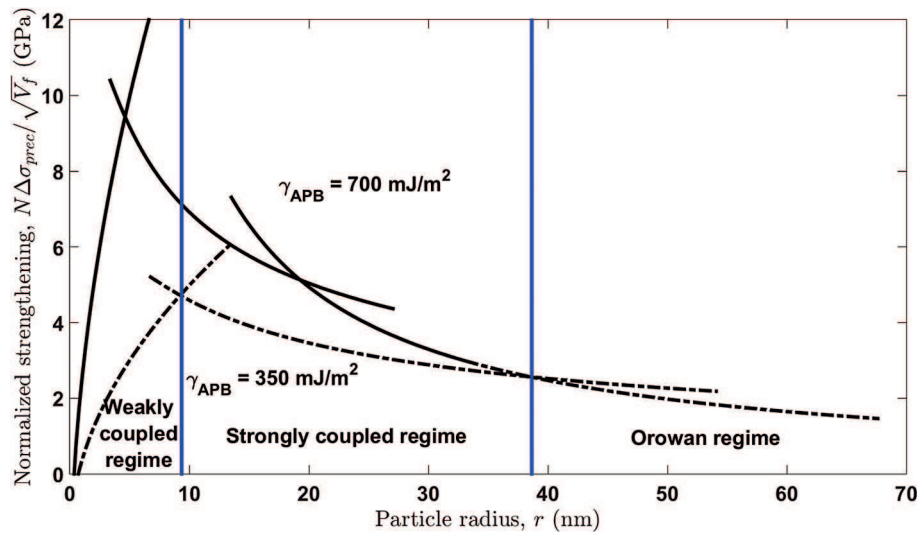


Fig. 12. Normalized ordered particle strengthening plotted as a function of the mean particle radius for γ_{APB} of 350 (dashed line) and 700 (solid line) mJ/m². The transition from weakly to strongly coupled particle shearing and the Orowan looping mechanism occurs earlier for higher values of γ_{APB} .

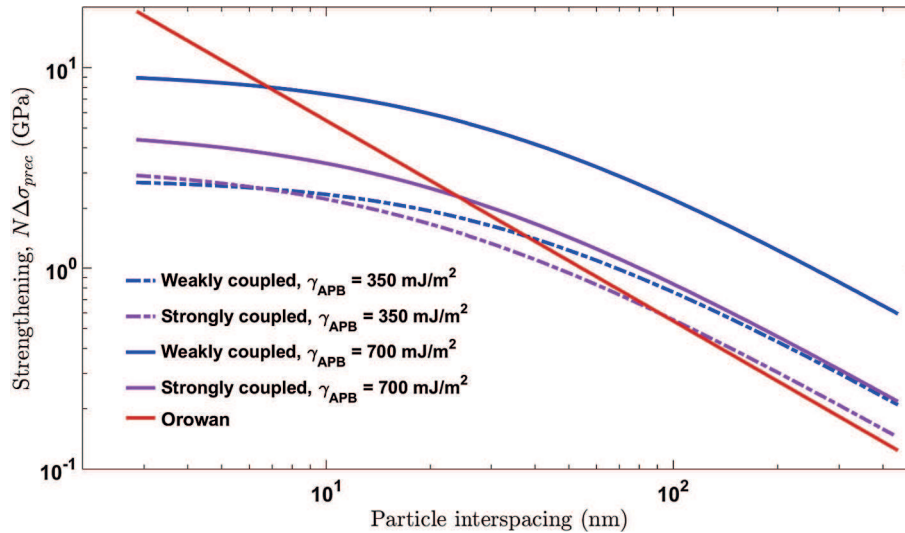


Fig. 13. Ordered particle strengthening plotted as a function of the channel spacing, at a fixed particle size of 10 nm, for different mechanisms for γ_{APB} of 350 (dashed line) and 700 (solid line) mJ/m², respectively.

spacing in front of the Orowan dislocation. Hence, to accommodate the large strain and fully percolative plasticity enabled in these alloys, dislocations must obviously overcome these topologically complex particle obstacle arrays predominantly by percolative shearing (Fig. 14(c and d)). Orowan looping might also contribute to the total shear, although to a much smaller extent than cutting, since macroscopic shape change requires complete percolative sweeping of shear planes.

An additional reason for the lower experimental yield strength increase by κ -carbide precipitation compared to the calculated value is the reduced concentration of alloying elements in the matrix due to κ -carbide formation. On the one hand, the solid solution strengthening of the matrix is reduced. On the other hand, the “depleted” matrix has a reduced tendency for short range ordering [24]. Both mechanisms reduce the effective strengthening contributed by precipitation hardening. It is difficult to quantitatively determine the effect of solid solution strengthening and strengthening by short range ordering in this highly alloyed

material. It is not clear if this can be treated like classical solid solution hardening or if ordering or clustering phenomena also contribute to strengthening in a non-linear fashion, especially in the AQ state. These contributions will be significantly reduced during aging due to solute element loss in the matrix.

In addition to the primary ordering strengthening, another contribution from the κ -carbide precipitation is the coherency strengthening due to the elastic strain field as a result of the lattice parameter difference between the κ -carbide precipitates and γ -matrix, which however is negligible as compared to the APB effect considering the low lattice misfit of the current alloy [21,22].

4.2. Strain hardening mechanisms

The plastic deformation mechanisms of high-Mn lightweight steels have been studied for many different alloy compositions [1,2,4]. Shear-band-induced plasticity (SIP) and microband-induced plasticity (MBIP) have been proposed to explain the good ductility

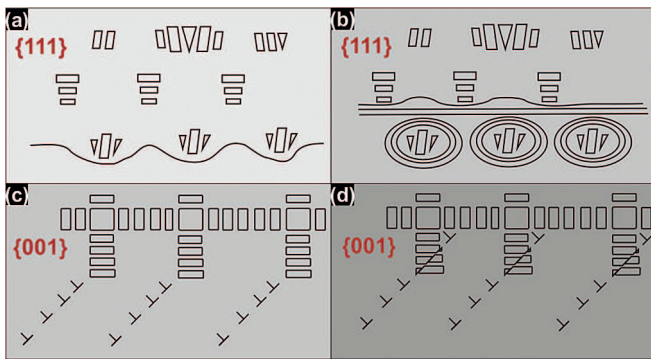


Fig. 14. Schematic illustration of the interaction of dislocations with κ -carbides. (a) At low strains, dislocation lines may bow into local broad γ -channels on the {111} slip planes where the morphology of κ -carbides are different from {001} views. (b) Orowan super-loops form around groups of κ -carbides and pile up in front of them as shown in (c), which is a view of this state on {001} planes. (d) Shearing of κ -carbides occurs when the pile-up stress is high enough to overcome the APB effect.

of these grades. Unlike crystallographic features, shear bands are macroscopic-scale non-crystallographic regions which can cross different orientations and grains [77]. Microbands are often observed at high strains as broad band-like structures composed of tangled dislocations with a very high density [2]. However, in the current alloy, we only observe crystallographically aligned and hence sharp slip bands following the conventional fcc slip system {110}<110>, even at high strains (Figs. 4–9). In contrast to shear bands or microbands, the slip bands are sharp, localized crystallographic slip regions along confined single slip planes. To substantiate the slip band formation, further high-resolution STEM analysis was performed. As shown in Fig. 15, the fully coherent ordered κ -carbides are evidenced by high angle annular dark field (HAADF) imaging. Some of them are sheared (Fig. 15(a)), which is found to occur along an atomically sharp plane (Fig. 15(b,c)). Therefore, it is safe to conclude that the formation of slip bands is responsible for the plasticity in the current alloy.

The evolution of the deformation microstructure in the present PH alloy is characterized by the refinement of slip bands during plastic straining. In the AQ state of the same alloy, similar

microstructural features were observed [24] and it was suggested that the total flow stress can be written as follows [78,79]:

$$\sigma_{\text{tot}}(\epsilon) = \sigma_0 + K \cdot M \cdot G \cdot b / D, \quad (8)$$

where K is a geometrical factor and D is the mean slip band spacing (Fig. 10). Contributions to the flow stress that do not depend on the deformation are summed in σ_0 . These are the Peierls-Nabarro lattice friction stress, solid solution strengthening, grain boundary strengthening, strengthening due to short-range order and precipitation hardening [78,79]. The latter term in equation (8) refers to the passing stress between dislocations, which increases with decreasing mean slip band spacing D .

Since similar deformation structure evolution as slip band refinement is found for the current alloy (Section 3.4), equation (8) is again adopted here for the evaluation of strain hardening capacity as in Ref. [24]. The stresses shown in Fig. 16 are calculated

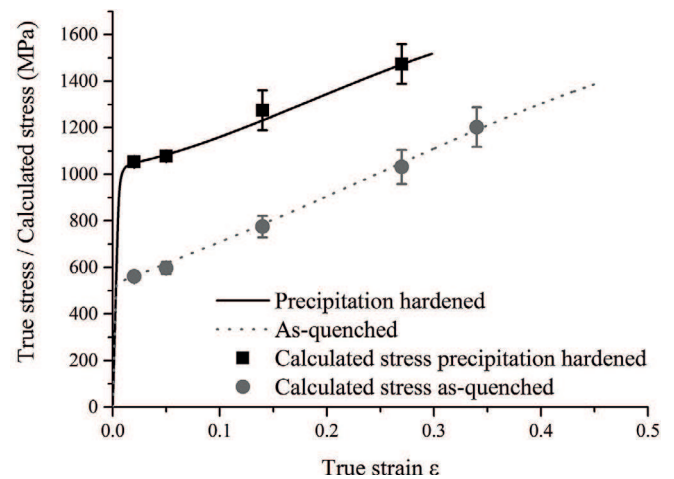


Fig. 16. True stress-strain curves of the precipitation-hardened material and the as-quenched state [24] along with the calculated stresses respectively. The calculated values in the present study were derived using the data from the slip band refinement analysis shown in Fig. 10. The increase of the flow stress compared to the as-quenched state is mainly attributed to the presence of shearable nano-sized κ -carbides.

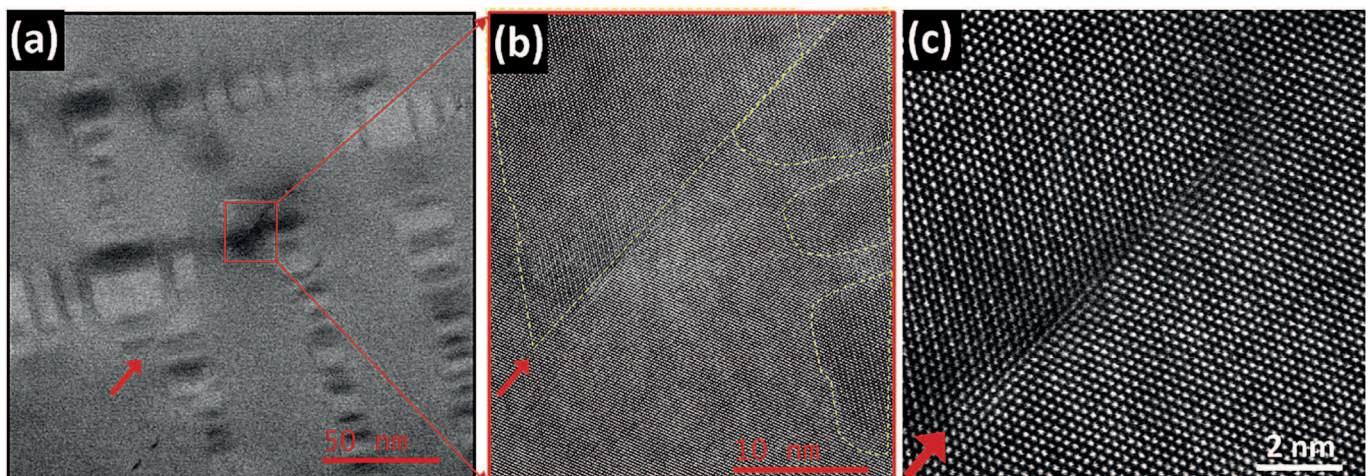


Fig. 15. STEM high angle annular dark field (HAADF) images of a sample strained to 0.05: (a) an overview image showing that a {111} slip band (dark line crossing the image from the lower left to the upper right corner) cuts through several κ -carbides, as indicated by the red arrow. (b) A magnified image of the red-outlined region in (a). The ordered κ -carbides with alternating rows of heavier (brighter) and lighter (darker) atoms are out-lined in yellow. The shearing of κ -carbide by an atomically sharp slip band is observed, which is even clear in the magnified (c) showing the still attached two parts of the sheared particle. (For interpretation of the references to colour in this figure legend, the reader is referred to the web version of this article.)

using equation (8) taking $\sigma_0 = 1020$ MPa (yield strength), a K-value of 1 and the D values as quantified in Fig. 10. The excellent agreement between the calculated values and the true stress-strain curve (Fig. 3) confirms that the observed dynamic slip band refinement is the main parameter governing the strain hardening behavior.

The influence of the κ -carbides on the strain hardening behavior of the PH alloy is hence best explained by an increased critical resolved shear stress due to the shearing process. Yet, the overall strain hardening mechanism does not seem to be otherwise strongly influenced by the presence of κ -carbides. We notice though that in Fig. 3 at low strains the strain hardening rate is lower than that of the AQ, viz. κ -free state, indicating that in addition to the positive strain hardening rate resulting from the dynamic slip band refinement the precipitates lead to a negative contribution to the overall strain hardening rate at low strains. Thus, local slip band softening might originate from shearing of the κ -carbides. Also, as manifested in Fig. 10, the slip band spacing refinement of the PH alloy is not as effective as that of AQ alloy, probably due to the obstacle effect of κ -carbide precipitates to slip band formation. Such an effect, especially at low strains (see Fig. 3 vs. Fig. 10) results in the lower strain hardening rate of the PH alloy.

We observe that upon deformation, the κ -carbides are not only sheared but also fragmented and dissolved and there are line segregations of solutes which are possibly dislocation lines according to the crystallographic analysis (Fig. 8). The minimum observed mean slip band distance at the strain level of 0.15 is around 250 nm, still larger than the average diameter of the κ -carbides (~ 20 nm). Therefore, on average, not all precipitates will be cut by dislocations and typically not more than one coplanar slip band is intersecting individual κ -carbides. However, as the strain increases, multiple slip bands are activated and at the intersection of slip bands κ -carbides get fragmented and dissolved (Figs. 6 and 7). The solute segregation to dislocation lines helps explaining the second strain hardening at high strains (Fig. 3).

A similar dissolution of shearable particles under plastic deformation has been reported in metals subjected to severe plastic deformation, e.g. dissolution of metastable fine precipitates in equal-channel angular pressed Al alloys [80,81], and in fatigued alloys, e.g. precipitate dissolution within the persistent slip bands or shear bands [82,83]. In those cases, the intense strain, either applied by severe deformation or accumulated by cycling, cut the particles into smaller nanoscale fragments, leading to the instability of the phase because of high surface energy and their eventual dissolution [84,85]. Such particle fragmentation is also observed in the present κ/γ alloy, driven by intersection of massive slip bands in high-strain states (Figs. 6, 7 and 9), which promotes the dissolution of κ -carbides.

It is known, on the other hand, that the dislocation interaction with solute atoms of precipitates might also cause the dissolution or decomposition of particles. One well-studied case is the cementite decomposition in heavily drawn pearlitic steels [86]. During the motion of dislocations, looping around the interfaces in that case, carbon atoms are dragged out of the cementite and segregate to dislocations. As for shearable particles, the penetration of dislocations through particles might lead to the transfer of interstitial atoms from the particles to the matrix due to drifting of atoms under the stress field of dislocations [87]. In the present case, the observed linear solute segregation are likely dislocations [32,88], the crystallographic orientations of which follows the typical fcc slip system (Fig. 8). A compositional analysis of such a segregation is illustrated in Fig. 17 using composition profiles as a function of the proximity to the selected interface (referred to as proximity histogram or proxigram [89]) and more conventional one-dimensional (1D) concentration profiles. Fig. 17(b) shows the

proxigram generated around the line segregations highlighted in purple in Fig. 17(a) by a 7.5 at.% C iso-concentration surface. The 1D concentration profiles from cylindrical regions of interest (ROIs) placed perpendicular to the dislocation lines, as shown in Fig. 17(a), are plotted in Fig. 17(c–d). Both methods clearly reveal the enrichment of C and Al to the dislocation lines, with enrichment factors of 2.8 and 1.2 respectively, in comparison to the neighborhood compositions. This result suggests that upon particle cutting, indeed the solutes of the κ -carbide precipitates are dragged along with the moving dislocations, which facilitates precipitate fragmentation and dissolution. Regarding the composition, no obvious difference is observed between the two solute-segregated dislocation lines in Fig. 17(c) and (d), which are probably of edge and mixed characters according to the analysis in Fig. 8(a) and (b), respectively.

4.3. Deformation structure evolution in the precipitation hardened alloy

In Ref. [24], a detailed discussion on the formation of slip bands and the gradual refinement of their average spacing during straining is provided for the case of the AQ state of the same alloy. In the preceding sections, we have shown that the governing strain hardening mechanism in the PH state is similar to that in the same alloy in the AQ state. Here, we discuss the dynamic slip band refinement mechanism for the case of an alloy containing κ -carbides and its effect on the overall strain hardening.

Following the discussion in Ref. [24], at the onset of plastic deformation dislocation loops are created by Frank-Read sources on {111} planes. With increasing strain the expanding dislocation loops leave the source, thereby destroying any kind of pre-existing chemical order on the respective glide plane. In the AQ state this was argued to be short-range order (SRO) and finely dispersed long-range-order (LRO) clusters. In the PH alloy chemically ordered κ -carbides are present, which are found to be sheared by dislocations (see Fig. 5).

These ordering features (SRO, LRO-clusters of κ -carbides) increase the stress needed for a dislocation to percolate a glide plane compared to an entirely disordered matrix. As the order on the glide plane is destroyed by the first dislocation on the respective glide plane, succeeding dislocations experience less resistance on the glide plane and will therefore stay on the same glide plane. This effect is referred to as “glide plane softening” [90–95]. It causes the pronounced planar glide, which in turn induces and promotes the formation of sharp crystallographic slip bands.

However, as the dislocations eventually reach the grain boundary, where they are blocked, or become stuck within the grain interior, the respective glide plane gradually fills-up with dislocations stemming from the same source. This increasing dislocation density on the same glide plane causes back stresses on the source, which eventually lead to its exhaustion. Hence, the piled-up dislocations lead to glide plane hardening. The slip band is then regarded as completely developed as it will emit only a few dislocations after it has been hardened by this mechanism.

In order to accommodate ongoing plastic deformation compliant with the external loading, new glide bands have to be generated. The increasing number of slip bands leads to a reduction of their spacing during straining, as quantified in Fig. 10. The reduction of the slip band spacing and the resulting passing stresses are shown to be the main contributions to strain hardening in the present material, see Fig. 16. Hence, the flow stress increases with increasing strain, which leads to a high strain hardening rate.

At high strains, the slip bands are getting gradually close enough to enable mutual annihilation of dislocations and/or the stress is high enough to allow cross slip, which also facilitates annihilation.

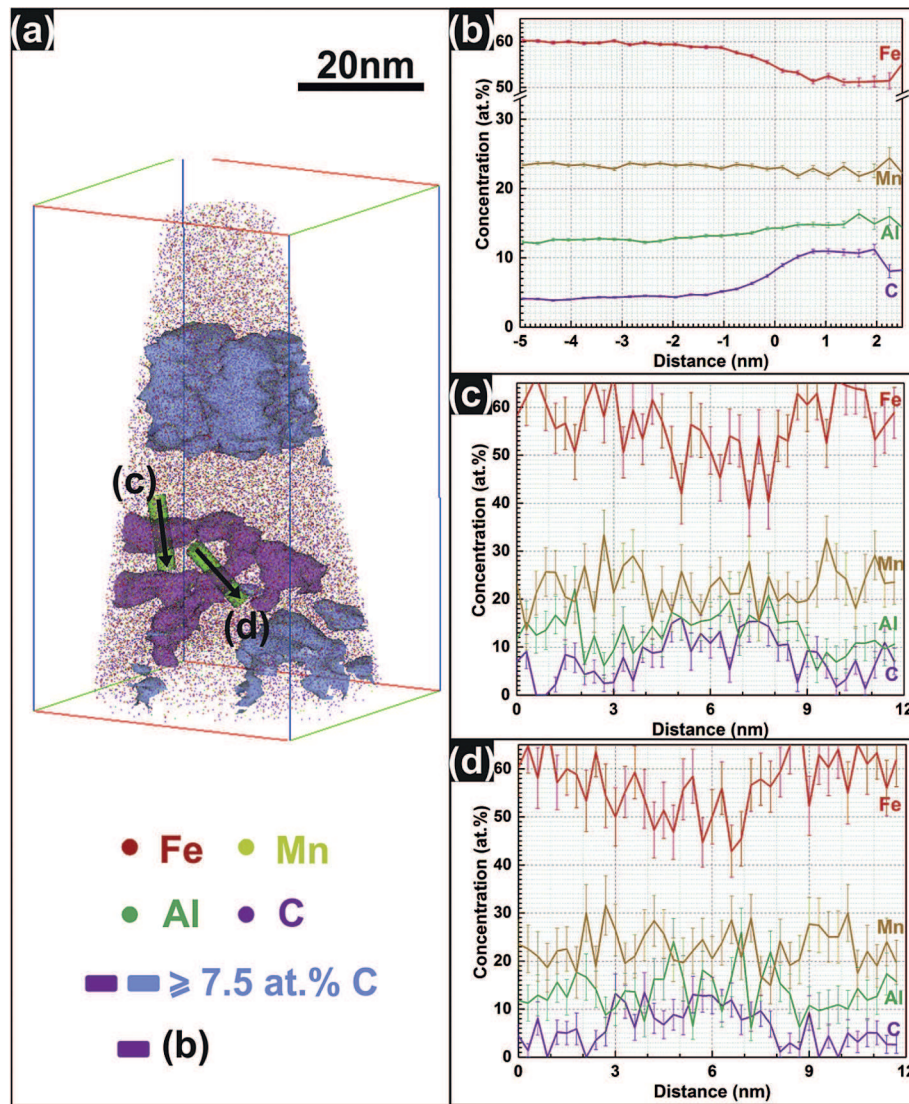


Fig. 17. Concentration analysis on solute segregation to dislocations: (b) Proxigram of the magenta-colored interface generated by a carbon iso-concentration surface of 7.5 at.% in (a). (c) (d) Two individual 1D concentration profiles of cylindrical regions of interest (ROIs) perpendicular to two dislocation lines as highlighted in (a). (For interpretation of the references to colour in this figure legend, the reader is referred to the web version of this article.)

Both effects, occurring most likely at large deformations and small slip band spacings, lead to dynamic recovery causing the reduction of the strain hardening rate at high strains. Failure takes place by ductile fracture after necking due to plastic instability. Because of the overall higher stress level in the PH material compared to the AQ state and lower strain hardening rate, this necking instability occurs in the PH alloy at a lower strain than in the AQ state as observed in the Considère-plot (Fig. 3). As a result, a lower uniform and total elongation of the precipitation-hardened material is measured.

In the framework of this discussion the effect of the presence of κ -carbides on the deformation behavior of the PH alloy is explained as follows: in newly generated slip bands dislocation loops expand and impinge κ -carbides. The first dislocation experiences high stresses due to the presence of chemical order in the crystal, may it be due to SRO or LRO or due to the κ -carbides. Both SRO zones and κ -carbides are sheared by dislocations (Fig. 5). In comparison to the AQ state where only very small ordered zones present (size < 2 nm [24]) the stress for the first dislocation to destroy the chemical order is strongly increased in the PH due to the presence of κ -

carbides. This, in turn, leads to an increased stress to form slip bands, which results in an increased yield strength. As new slip bands are generated dynamically in the non-sheared zones between already existing slip bands, they also shear the precipitate structure. Hence, the same increased stress is expected for newly generated slip bands. As this argumentation applies to all newly generated slip bands at all strain levels, it translates into an increased flow stress of the PH material compared to the AQ state. The gradual refinement of the slip band structure during straining leads surprisingly to strain hardening in a similar fashion as in the AQ state. As a result, an increased flow stress is expected due to the cutting of κ -carbides, compared to the AQ state. The increased flow stress in conjunction with the observed structure refinement proves the dynamic slip band refinement as effective strain hardening mechanism in the studied material. The resulting strain hardening rate is high enough to compensate the negative strain hardening rate by shearing and fragmenting the κ -carbide precipitates by dislocations and the additional effect of dragging out carbon and other elements by moving dislocations which leads to a reduction of the APB energy in κ -carbides.

5. Conclusions

In this work, we have studied the strengthening and strain hardening mechanisms of the precipitation hardened high-Mn steel (Fe-30.4Mn-8Al-1.2C, wt.%). The presence of nano-sized κ carbides (size about 20 nm) has been confirmed by TEM and APT. A detailed ECCI, TEM and correlative TEM/APT analysis at different strains has been conducted in order to evaluate the deformation microstructure and its evolution during straining. The following conclusions are drawn:

- The ordered κ -carbide precipitates are inhomogeneously arranged in 3D space with both, broad and narrow γ channels separating them.
- With the presence of κ -carbides, the precipitation hardened material exhibits an increase in yield strength of about 480 MPa compared to the as-quenched state and an outstanding combination of strength and ductility (yield strength = 1020 MPa, ultimate tensile strength = 1125 MPa, uniform elongation = 36%, total elongation = 41%).
- The κ -carbide precipitates are primarily sheared by gliding dislocations along sharp crystallographic slip bands during deformation. $\{111\}<110>$ slip systems are activated. Fragmentation and dissolution of κ -carbides are observed at high strains along with solute segregations of Al and C to linear features which are most likely dislocation lines.
- The primary strengthening mechanism is ordering strengthening. The APB energy of the ordered κ -carbides has been estimated by DFT calculations and found to be strongly related to the C concentration of the particles. A quantitative evaluation of the strengthening contribution by κ -carbide precipitates has been made, which is higher than the actually observed strength contribution in the alloy. This was explained by the formation of dislocation pile-ups and matrix solid solution loss during precipitation. The activation of different strengthening mechanisms upon different microstructure parameters has been discussed.
- The main strain hardening mechanism is dynamic slip band refinement during straining. The spacing between slip bands is reduced as strain increases which leads to an increase in the dislocation passing stresses. As a result the precipitation-hardened material shows strong strain hardening, which however is lower than the same materials in as-quenched state due to weaker slip band spacing refinement in the presence of precipitates and local slip band softening as a result of particle shearing. Solute segregation to potential dislocations upon particle dissolution at high strains might also contribute to the strain hardening at high strains.

Acknowledgements

The authors acknowledge funding of this project by the German Research Foundation [Deutsche Forschungsgemeinschaft (DFG)] through SFB 761 “Steel Ab Initio”.

References

- [1] G. Frommeyer, U. Brueck, Microstructures and mechanical properties of high-strength Fe-Mn-Al-C light-weight TRIPLEX steels, *Steel Res. Int.* 77 (9–10) (2006) 627–633.
- [2] K.-T. Park, Tensile deformation of low-density Fe-Mn-Al-C austenitic steels at ambient temperature, *Scr. Mater.* 68 (6) (2013) 375–379.
- [3] H. Springer, D. Raabe, Rapid alloy prototyping: compositional and thermo-mechanical high throughput bulk combinatorial design of structural materials based on the example of 30Mn–1.2 C–xAl triplex steels, *Acta Mater.* 60 (12) (2012) 4950–4959.
- [4] I. Gutierrez-Urrutia, D. Raabe, Influence of Al content and precipitation state on the mechanical behavior of austenitic high-Mn low-density steels, *Scr. Mater.* 68 (6) (2013) 343–347.
- [5] H. Kim, D.-W. Suh, N.J. Kim, Fe-Al-Mn-C lightweight structural alloys: a review on the microstructures and mechanical properties, *Sci. Technol. Adv. Mater.* 14 (1) (2013) 014205.
- [6] K. Choi, C.-H. Seo, H. Lee, S. Kim, J.H. Kwak, K.G. Chin, K.-T. Park, N.J. Kim, Effect of aging on the microstructure and deformation behavior of austenite base lightweight Fe–28Mn–9Al–0.8 C steel, *Scr. Mater.* 63 (10) (2010) 1028–1031.
- [7] K.M. Chang, C.G. Chao, T.F. Liu, Excellent combination of strength and ductility in an Fe–9Al–28Mn–1.8 C alloy, *Scr. Mater.* 63 (2) (2010) 162–165.
- [8] C.L. Lin, C.G. Chao, H.Y. Bor, T.F. Liu, Relationship between microstructures and tensile properties of an Fe-30 Mn-8.5 Al-2.0 C alloy, *Mater. Trans.* 51 (6) (2010) 1084–1088.
- [9] L.N. Bartlett, D.C. Van Aken, J. Medvedeva, D. Isheim, N.I. Medvedeva, K. Song, An atom probe study of kappa carbide precipitation and the effect of silicon addition, *Metall. Mater. Trans. A* 45 (2014) 2421–2435.
- [10] K. Sato, K. Tagawa, Y. Inoue, Age hardening of an Fe-30Mn-9Al-0.9 C alloy by spinodal decomposition, *Scr. Metall. Mater.* 22 (6) (1988) 899–902.
- [11] S. Tjong, Electron microscope observations of phase decompositions in an austenitic Fe-8.7 Al-29.7 Mn-1.04 C alloy, *Mater. Charact.* 24 (3) (1990) 275–292.
- [12] K. Ishida, H. Ohtani, N. Satoh, R. Kainuma, T. Nishizawa, Phase equilibria in Fe-Mn-Al-C alloys, *ISIJ Int.* 30 (8) (1990) 680–686.
- [13] W.K. Choo, J.H. Kim, J.C. Yoon, Microstructural change in austenitic Fe-30.0 wt % Mn-7.8 wt% Al-1.3 wt% C initiated by spinodal decomposition and its influence on mechanical properties, *Acta Mater.* 45 (12) (1997) 4877–4885.
- [14] K. Sato, K. Tagawa, Y. Inoue, Modulated structure and magnetic properties of age-hardenable Fe-Mn-Al-C alloys, *Metall. Trans. A* 21 (1) (1990) 5–11.
- [15] M. Koyama, H. Springer, S.V. Merzlikin, K. Tsuzaki, E. Akiyama, D. Raabe, Hydrogen embrittlement associated with strain localization in a precipitation-hardened Fe–Mn–Al–C light weight austenitic steel, *Int. J. Hydrogen Energy* 39 (2014) 4634–4646.
- [16] M.C. Ha, J.-M. Koo, J.-K. Lee, S.W. Hwang, K.-T. Park, Tensile deformation of a low density Fe–27Mn–12Al–0.8 C duplex steel in association with ordered phases at ambient temperature, *Mater. Sci. Eng. A* 586 (2013) 276–283.
- [17] K.-T. Park, S.W. Hwang, C.Y. Son, J.-K. Lee, Effects of heat treatment on microstructure and tensile properties of a Fe-27Mn-12Al-0.8 C low-density steel, *JOM J. Miner. Metals Mater. Soc.* 66 (9) (2014) 1828–1836.
- [18] K. Sato, K. Tagawa, Y. Inoue, Spinodal decomposition and mechanical properties of an austenitic Fe-30wt.% Mn-9wt.% Al-0.9 wt.% C alloy, *Mater. Sci. Eng. A* 111 (1989) 45–50.
- [19] M. Yao, P. Dey, J.-B. Seol, P. Choi, M. Herbig, R. Marceau, T. Hickel, J. Neugebauer, D. Raabe, Combined atom probe tomography and density functional theory investigation of the Al off-stoichiometry of κ -carbides in an austenitic Fe–Mn–Al–C low density steel, *Acta Mater.* 106 (2016) 229–238.
- [20] P. Dey, R. Nazarov, B. Dutta, M.J. Yao, M. Herbig, M. Friák, T. Hickel, D. Raabe, J. Neugebauer, Ab initio explanation of disorder and off-stoichiometry in Fe-Mn-Al-C κ -carbides, *Phys. Rev. B* 95 (10) (2017).
- [21] M.J. Yao, κ -carbide in a High-Mn Light-weight Steel: Precipitation, Off-stoichiometry and Deformation (Doctoral dissertation). Under publication, 2017.
- [22] W. Song, W. Zhang, J. von Appen, R. Dronskowski, W. Bleck, κ -phase formation in Fe–Mn–Al–C austenitic steels, *Steel Res. Int.* 86 (10) (2015) 1161–1169.
- [23] C. Chao, L. Hwang, T. Liu, Spinodal decomposition in Fe–9.0 Al-30.5 Mn-xC alloys, *Scripta Metall. Mater.* 29 (5) (1993) 647–650.
- [24] E. Welsch, D. Ponge, S.H. Haghighat, S. Sandlöbes, P. Choi, M. Herbig, S. Zaefferer, D. Raabe, Strain hardening by dynamic slip band refinement in a high-Mn lightweight steel, *Acta Mater.* 116 (2016) 188–199.
- [25] Z. Wu, H. Ding, X. An, D. Han, X. Liao, Influence of Al content on the strain-hardening behavior of aged low density Fe–Mn–Al–C steels with high Al content, *Mater. Sci. Eng. A* 639 (2015) 187–191.
- [26] I. Gutierrez-Urrutia, D. Raabe, High strength and ductile low density austenitic FeMnAlC steels: simplex and alloys strengthened by nanoscale ordered carbides, *Mater. Sci. Technol.* 30 (9) (2014) 1099–1104.
- [27] S. Zaefferer, N.-N. Elhami, Theory and application of electron channelling contrast imaging under controlled diffraction conditions, *Acta Mater.* 75 (2014) 20–50.
- [28] I. Gutierrez-Urrutia, S. Zaefferer, D. Raabe, Electron channeling contrast imaging of twins and dislocations in twinning-induced plasticity steels under controlled diffraction conditions in a scanning electron microscope, *Scr. Mater.* 61 (7) (2009) 737–740.
- [29] Y. Toji, H. Matsuda, M. Herbig, P.-P. Choi, D. Raabe, Atomic-scale analysis of carbon partitioning between martensite and austenite by atom probe tomography and correlative transmission electron microscopy, *Acta Mater.* 65 (2014) 215–228.
- [30] K. Thompson, D. Lawrence, D.J. Larson, J.D. Olson, T.F. Kelly, B. Gorman, In situ site-specific specimen preparation for atom probe tomography, *Ultramicroscopy* 107 (2–3) (2007) 131–139.
- [31] J.-B. Seol, S.-H. Na, B. Gault, J.-E. Kim, J.-C. Han, C.-G. Park, D. Raabe, Core-shell nanoparticle arrays double the strength of steel, *Sci. Rep.* 7 (2017).
- [32] M. Kuzmina, M. Herbig, D. Ponge, S. Sandlöbes, D. Raabe, Linear complexes: confined chemical and structural states at dislocations, *Science* 349 (6252) (2015) 1080–1083.
- [33] M. Herbig, D. Raabe, Y. Li, P. Choi, S. Zaefferer, S. Goto, Atomic-scale quantification of grain boundary segregation in nanocrystalline material, *Phys. Rev. Lett.* 112 (12) (2014) 126103.
- [34] M. Herbig, Spatially correlated electron microscopy and atom probe

- tomography: current possibilities and future perspectives, *Scr. Mater.* (2017) in press.
- [35] I. Gutierrez-Urrutia, S. Zaefferer, D. Raabe, Coupling of electron channeling with EBSD: toward the quantitative characterization of deformation structures in the SEM, *Jom* 65 (9) (2013) 1229–1236.
 - [36] A. Kovács, R. Schierholz, K. Tillmann, FEI titan G2 80-200 CREWLEY, J. Large-scale Res. Facil. 2 (A43) (2016) 1–4.
 - [37] M. Herbig, P. Choi, D. Raabe, Combining structural and chemical information at the nanometer scale by correlative transmission electron microscopy and atom probe tomography, *Ultramicroscopy* 153 (2015) 32–39.
 - [38] R.K. Marceau, I. Gutierrez-Urrutia, M. Herbig, K.L. Moore, S. Lozano-Perez, D. Raabe, Multi-scale correlative microscopy investigation of both structure and chemistry of deformation twin bundles in Fe–Mn–C steel, *Microsc. Microanal.* 19 (06) (2013) 1581–1585.
 - [39] A. Stoffers, O. Joczaru-Miréidin, W. Seifert, S. Zaefferer, S. Riepe, D. Raabe, Grain boundary segregation in multicrystalline silicon: correlative characterization by EBSD, EBC, and atom probe tomography, *Prog. Photovoltaics Res. Appl.* 23 (12) (2015) 1742–1753.
 - [40] C. Hwang, C. Chao, T. Liu, Grain boundary precipitation in an Fe-8.0 Al-31.5 Mn-1.05 C alloy, *Scripta Metall. Mater.* 28 (2) (1993) 263–268.
 - [41] K. Yang, W. Choo, Evidence of carbon ordering and morphology change in a cubic carbide phase, *Philos. Mag. Lett.* 62 (3) (1990) 221–226.
 - [42] H. Huang, D. Gan, P. Kao, Effect of alloying additions on the κ phase precipitation in austenitic Fe–Mn–Al–C alloys, *Scripta Metall. Mater.* 30 (4) (1994) 499–504.
 - [43] R. You, P.-W. Kao, D. Gan, Mechanical properties of Fe-30Mn-10Al-1C-1Si alloy, *Mater. Sci. Eng. A* 117 (1989) 141–148.
 - [44] A.J. Ardell, R.B. Nicholson, On the modulated structure of aged Ni–Al alloys: with an Appendix on the elastic interaction between inclusions by JD Eshelby, Cavendish Laboratory, University of Cambridge, England, *Acta Metall.* 14 (10) (1966) 1295–1309.
 - [45] C. Monier, C. Bertrand, J.-P. Dallas, M.-F. Trichet, M. Cornet, P. Veyssiére, Transmission electron microscopy analysis of the early stages of damage in a γ/γ' nickel-based alloy under low cycle fatigue, *Mater. Sci. Eng. A* 188 (1) (1994) 133–139.
 - [46] J. Sato, T. Omori, K. Oikawa, I. Ohnuma, R. Kainuma, K. Ishida, Cobalt-base high-temperature alloys, *Science* 312 (5770) (2006) 90–91.
 - [47] A. Suzuki, T.M. Pollock, High-temperature strength and deformation of γ/γ' two-phase Co–Al–W-based alloys, *Acta Mater.* 56 (6) (2008) 1288–1297.
 - [48] T. Pollock, J. Dibbern, M. Tsunekane, J. Zhu, A. Suzuki, New Co-based γ – γ' high-temperature alloys, *JOM* 62 (1) (2010) 58–63.
 - [49] P. Gregson, H. Flower, Microstructural control of toughness in aluminium–lithium alloys, *Acta Metall.* 33 (3) (1985) 527–537.
 - [50] F. Sun, J. Tong, Q. Feng, J. Zhang, Microstructural evolution and deformation features in gas turbine blades operated in-service, *J. Alloy. Compd.* 618 (2015) 728–733.
 - [51] M. Petreñec, K. Obrtlík, J. Polák, Inhomogeneous dislocation structure in fatigued INCONEL 713 LC superalloy at room and elevated temperatures, *Mater. Sci. Eng. A* 400 (2005) 485–488.
 - [52] X. Lv, F. Sun, J. Tong, Q. Feng, J. Zhang, Paired dislocations and their interactions with γ' particles in polycrystalline superalloy GH4037, *J. Mater. Eng. Perform.* 24 (1) (2015) 143–148.
 - [53] X. Lv, F. Sun, J. Tong, S. Zhang, Q. Feng, J. Zhang, Dislocation configurations and stress distribution along the transverse Axis of turbine blade body, *J. Mater. Eng. Perform.* 24 (12) (2015) 4620–4625.
 - [54] H. Aboulfadl, J. Deges, P. Choi, D. Raabe, Dynamic strain aging studied at the atomic scale, *Acta Mater.* 86 (2015) 34–42.
 - [55] Y. Li, D. Raabe, M. Herbig, P.-P. Choi, S. Goto, A. Kostka, H. Yarita, C. Borchers, R. Kirchheim, Segregation stabilizes nanocrystalline bulk steel with near theoretical strength, *Phys. Rev. Lett.* 113 (10) (2014) 106104.
 - [56] D. Raabe, P.-P. Choi, Y. Li, A. Kostka, X. Sauvage, F. Lecouturier, K. Hono, R. Kirchheim, R. Pippan, D. Embury, Metallic composites processed via extreme deformation: toward the limits of strength in bulk materials, *Mrs Bull.* 35 (12) (2010) 982–991.
 - [57] R. Kirchheim, Reducing grain boundary, dislocation line and vacancy formation energies by solute segregation: II. Experimental evidence and consequences, *Acta Mater.* 55 (15) (2007) 5139–5148.
 - [58] Y. Li, P. Choi, C. Borchers, S. Westerkamp, S. Goto, D. Raabe, R. Kirchheim, Atomic-scale mechanisms of deformation-induced cementite decomposition in pearlite, *Acta Mater.* 59 (10) (2011) 3965–3977.
 - [59] S. Djaziri, Y. Li, G. Nematollahi, B. Grabowski, S. Goto, C. Kirchlechner, A. Kostka, S. Doyle, J. Neugebauer, D. Raabe, Deformation-induced martensite: a new paradigm for exceptional steels, *Adv. Mater.* 28 (35) (2016) 7753–7757.
 - [60] C.C. Tasan, M. Diehl, D. Yan, C. Zambaldi, P. Shanthraj, F. Roters, D. Raabe, Integrated experimental–simulation analysis of stress and strain partitioning in multiphase alloys, *Acta Mater.* 81 (2014) 386–400.
 - [61] D. Raabe, M. Sachtleber, Z. Zhao, F. Roters, S. Zaefferer, Micromechanical and macromechanical effects in grain scale polycrystal plasticity experimentation and simulation, *Acta Mater.* 49 (17) (2001) 3433–3441.
 - [62] Z. Zhao, M. Ramesh, D. Raabe, A. Cuitino, R. Radovitzky, Investigation of three-dimensional aspects of grain-scale plastic surface deformation of an aluminum oligocrystal, *Int. J. Plast.* 24 (12) (2008) 2278–2297.
 - [63] M. Sachtleber, Z. Zhao, D. Raabe, Experimental investigation of plastic grain interaction, *Mater. Sci. Eng. A* 336 (1) (2002) 81–87.
 - [64] G. Gottstein, *Physical Foundations of Materials Science*, Springer, Berlin, 2004.
 - [65] A. Ardell, Precipitation hardening, *Metall. Trans. A* 16 (12) (1985) 2131–2165.
 - [66] R.C. Reed, *The Superalloys: Fundamentals and Applications*, Cambridge university press, 2008.
 - [67] R. Stoller, S. Zinkle, On the relationship between uniaxial yield strength and resolved shear stress in polycrystalline materials, *J. Nucl. Mater.* 283 (2000) 349–352.
 - [68] G. Kresse, J. Furthmüller, Efficient iterative schemes for ab initio total-energy calculations using a plane-wave basis set, *Phys. Rev. B* 54 (16) (1996) 11169.
 - [69] P.E. Blöchl, Projector augmented-wave method, *Phys. Rev. B* 50 (24) (1994) 17953.
 - [70] K. Burke, J. Perdew, M. Ernzerhof, Generalized gradient approximation made simple [Phys. Rev. Lett. 77, 3865 (1996)], *Phys. Rev. Lett.* 78 (1997) 1396.
 - [71] T. Hickel, A. Dick, B. Grabowski, F. Körmann, J. Neugebauer, Steel design from fully parameter-free Ab initio computer simulations, *Steel Res. Int.* 80 (1) (2009) 4–8.
 - [72] I. Bleskov, T. Hickel, J. Neugebauer, A. Ruban, Impact of local magnetism on stacking fault energies: a first-principles investigation for fcc iron, *Phys. Rev. B* 93 (21) (2016) 214115.
 - [73] H. Idrissi, L. Ryelandt, M. Veron, D. Schryvers, P. Jacques, Is there a relationship between the stacking fault character and the activated mode of plasticity of Fe–Mn-based austenitic steels? *Scr. Mater.* 60 (11) (2009) 941–944.
 - [74] T. Hickel, S. Sandlöbes, R.K. Marceau, A. Dick, I. Bleskov, J. Neugebauer, D. Raabe, Impact of nanodiffusion on the stacking fault energy in high-strength steels, *Acta Mater.* 75 (2014) 147–155.
 - [75] D.R. Steinmetz, T. Jäpel, B. Wietbrock, P. Eisenlohr, I. Gutierrez-Urrutia, A. Saeed-Akbari, T. Hickel, F. Roters, D. Raabe, Revealing the strain-hardening behavior of twinning-induced plasticity steels: theory, simulations, experiments, *Acta Mater.* 61 (2) (2013) 494–510.
 - [76] D. Raabe, F. Roters, J. Neugebauer, I. Gutierrez-Urrutia, T. Hickel, W. Bleck, J.M. Schneider, J.E. Wittig, J. Mayer, Ab initio-guided design of twinning-induced plasticity steels, *Mrs Bull.* 41 (04) (2016) 320–325.
 - [77] N. Jia, P. Eisenlohr, F. Roters, D. Raabe, X. Zhao, Orientation dependence of shear banding in face-centered-cubic single crystals, *Acta Mater.* 60 (8) (2012) 3415–3434.
 - [78] D. Kuhlmann-Wilsdorf, H. Wilsdorf, J. Wert, LEDS theory of workhardening stages and “planar” versus “distributed” glide, *Scripta Metall. Mater.* 31 (6) (1994) 729–734.
 - [79] U. Kocks, H. Mecking, Physics and phenomenology of strain hardening: the FCC case, *Prog. Mater. Sci.* 48 (3) (2003) 171–273.
 - [80] M. Murayama, Z. Horita, K. Hono, Microstructure of two-phase Al–1.7 at% Cu alloy deformed by equal-channel angular pressing, *Acta Mater.* 49 (1) (2001) 21–29.
 - [81] I. Gutierrez-Urrutia, M. Munoz-Morris, D.G. Morris, The effect of coarse second-phase particles and fine precipitates on microstructure refinement and mechanical properties of severely deformed Al alloy, *Mater. Sci. Eng. A* 394 (1) (2005) 399–410.
 - [82] W. Vogel, M. Wilhelm, V. Gerold, Persistent slip bands in fatigued peak aged Al–Zn–Mg single crystals—II. Persistent slip bands in front of stage I fatigue cracks, *Acta Metall.* 30 (1) (1982) 31–35.
 - [83] A. Vinogradov, V. Patlan, Y. Suzuki, K. Kitagawa, V. Kopylov, Structure and properties of ultra-fine grain Cu–Cr–Zr alloy produced by equal-channel angular pressing, *Acta Mater.* 50 (7) (2002) 1639–1651.
 - [84] W. Guo, E.A. Jägle, P.-P. Choi, J. Yao, A. Kostka, J.M. Schneider, D. Raabe, Shear-induced mixing governs codeformation of crystalline-amorphous nanolaminates, *Phys. Rev. Lett.* 113 (3) (2014) 035501.
 - [85] W. Guo, J. Yao, E.A. Jägle, P.-P. Choi, M. Herbig, J.M. Schneider, D. Raabe, Deformation induced alloying in crystalline–metallic glass nano-composites, *Mater. Sci. Eng. A* 628 (2015) 269–280.
 - [86] Y. Li, P. Choi, C. Borchers, Y. Chen, S. Goto, D. Raabe, R. Kirchheim, Atom probe tomography characterization of heavily cold drawn pearlitic steel wire, *Ultramicroscopy* 111 (6) (2011) 628–632.
 - [87] V. Sagaradze, V. Shabashov, Deformation-induced anomalous phase transformations in nanocrystalline FCC Fe–Ni based alloys, *Nanostruct. Mater.* 9 (1) (1997) 681–684.
 - [88] G. Smith, D. Hudson, P. Styman, C. Williams, Studies of dislocations by field ion microscopy and atom probe tomography, *Philos. Mag.* 93 (28–30) (2013) 3726–3740.
 - [89] O.C. Hellman, J.A. Vandenbroucke, J. Rüsing, D. Isheim, D.N. Seidman, Analysis of three-dimensional atom-probe data by the proximity histogram, *Microsc. Microanal.* 6 (05) (2000) 437–444.
 - [90] J.D. Yoo, K.-T. Park, Microband-induced plasticity in a high Mn–Al–C light steel, *Mater. Sci. Eng. A* 496 (1) (2008) 417–424.
 - [91] J.K. Kim, L. Chen, H.S. Kim, S.K. Kim, G.S. Kim, Y. Estrin, B. De Cooman, Strain rate sensitivity of C-alloyed, High-Mn, twinning-induced plasticity steel, *Steel Res. Int.* 80 (7) (2009) 493–498.
 - [92] K.-T. Park, K.G. Jin, S.H. Han, S.W. Hwang, K. Choi, C.S. Lee, Stacking fault energy and plastic deformation of fully austenitic high manganese steels: effect of Al addition, *Mater. Sci. Eng. A* 527 (16) (2010) 3651–3661.
 - [93] J. Olfe, H. Neuhäuser, Dislocation groups, multipoles, and friction stresses in α -CuZn alloys, *Phys. Status Solid.* A 109 (1) (1988) 149–160.
 - [94] G. Saller, K. Spiradek-Hahn, C. Scheu, H. Clemens, Microstructural evolution of Cr–Mn–N austenitic steels during cold work hardening, *Mater. Sci. Eng. A* 427 (1) (2006) 246–254.
 - [95] V. Gerold, H.P. Karnthaler, On the origin of planar slip in fcc alloys, *Acta Metall.* 37 (8) (1989) 2177–2183.